JM PAPERS

Comparing local energy cascade rates in isotropic turbulence using structure-function and filtering formulations

Hanxun Yao[1],†, Michael Schnaubelt[2], Alexander S. Szalay[2], Tamer A. Zaki[1] and Charles Meneveau[1]

[1]Department of Mechanical Engineering & The Institute for Data Intensive Engineering and Science, Johns Hopkins University, Baltimore, MD 21218, USA

[2]Department of Physics and Astronomy & The Institute for Data Intensive Engineering and Science, Johns Hopkins University, Baltimore, MD 21218, USA

Two common definitions of the spatially local rate of kinetic energy cascade at some scale ℓ in turbulent flows are (i) the cubic velocity difference term appearing in the 'scale-integrated local Kolmogorov–Hill' equation (structure-function approach), and (ii) the subfilter-scale energy flux term in the transport equation for subgrid-scale kinetic energy (filtering approach). We perform a comparative study of both quantities based on direct numerical simulation data of isotropic turbulence at Taylor-scale Reynolds number 1250. While in the past observations of negative subfilter-scale energy flux (backscatter) have led to debates regarding interpretation and relevance of such observations, we argue that the interpretation of the local structure-function-based cascade rate definition is unambiguous since it arises from a divergence term in scale space. Conditional averaging is used to explore the relationship between the local cascade rate and the local filtered viscous dissipation rate as well as filtered velocity gradient tensor properties such as its invariants. We find statistically robust evidence of inverse cascade when both the large-scale rotation rate is strong and the large-scale strain rate is weak. Even stronger net inverse cascading is observed in the 'vortex compression' $R > 0$, $Q > 0$ quadrant, where R and Q are velocity gradient invariants. Qualitatively similar but quantitatively much weaker trends are observed for the conditionally averaged subfilter-scale energy flux. Flow visualizations show consistent trends, namely that spatially, the inverse cascade events appear to be located within large-scale vortices, specifically in subregions when R is large.

Key words: turbulence theory, isotropic turbulence

† Email address for correspondence: hyao12@jhu.edu

980 A42-1

H. Yao, M. Schnaubelt, A.S. Szalay, T.A. Zaki and C. Meneveau

1. Introduction

The classic description of the energy cascade in turbulence postulates that kinetic energy originates from forcing large-scale eddies, is transferred subsequently to smaller-scale eddies (forward cascade), and is dissipated eventually due to viscous effects (Richardson 1922; Kolmogorov 1941). In a statistical sense, the sign and magnitude of third-order moments of velocity increments confirm this general direction of the energy cascade, as described by the 4/5 law governing the global average of the third-order longitudinal velocity increment (Kolmogorov 1941; Frisch 1995), $\langle \delta u_L(\ell)^3 \rangle \equiv \langle ([\boldsymbol{u}(\boldsymbol{x}+\boldsymbol{\ell}) - \boldsymbol{u}(\boldsymbol{x})] \cdot \boldsymbol{\ell}/\ell)^3 \rangle = -\frac{4}{5}\ell\langle\epsilon\rangle$, where $\langle\cdot\rangle$ denotes global averaging, $\delta u_L(\ell)$ is the longitudinal velocity increment, and ϵ is the viscous dissipation rate, while the displacement $\ell = |\boldsymbol{\ell}|$ is assumed to be well inside the inertial range of turbulence. In this sense, the quantity $-\frac{5}{4}\langle \delta u_L(\ell)^3 \rangle/\ell$ is often interpreted as a measure of the energy flux going from scales larger than ℓ to all smaller scales. Because turbulence is known to be highly intermittent in space and time (Kolmogorov 1962; Meneveau & Sreenivasan 1991; Frisch 1995), there has also been much interest in characterizing the local properties of the energy cascade, i.e. the fluctuations of the energy flux before averaging. However, without statistical averaging, the 4/5 law is less meaningful, e.g. the quantity $-\frac{5}{4}\delta u_L^3/\ell$ cannot simply be interpreted as an energy flux locally in space and time. To enable such interpretation, it is necessary to consider explicit angular averaging over all possible directions of the vector $\boldsymbol{\ell}$. Such formulations have been developed in prior works by Duchon & Robert (2000), Eyink (2002) and Hill (2001, 2002). Duchon & Robert (2000) and Eyink (2002) use such equations to study the energy cascade and energy dissipation in the limit of zero viscosity. A review about extensions to the classic Kolmogorov equation is presented by Dubrulle (2019), focusing specifically on the Duchon & Robert (2000) local formulation.

Hill (2001, 2002) developed a local version of the Kolmogorov equation in which the reference position $\boldsymbol{x}$ is located symmetrically halfway between the two points $\boldsymbol{x} + \boldsymbol{r}/2$ and $\boldsymbol{x} - \boldsymbol{r}/2$ separated by $\boldsymbol{r}$ over which the velocity increment is computed. This equation, which we will denote as the Kolmogorov–Hill (KH) equation – sometimes also called the Kármán–Howarth–Monin–Hill (Danaila *et al.* 2012; Yasuda & Vassilicos 2018) or generalized Kolmogorov (Marati, Casciola & Piva 2004) equation) – describes the evolution of the second-order (squared) velocity difference, a measure of energy content of all scales smaller than $|\boldsymbol{r}|$ at a specific physical position $\boldsymbol{x}$. As will be reviewed in § 2, scale-space integration over $\boldsymbol{r}$ of the KH equation up to some scale ℓ in the inertial range and without additional statistical averaging provides a localized description of the energy cascade process (Hill 2002; Yasuda & Vassilicos 2018). The KH equation also includes effects of viscous dissipation, viscous diffusion, advection and pressure. A number of prior works have studied various versions of the KH equation. For isotropic turbulence, Yasuda & Vassilicos (2018) quantified the variability of the energy flux that arises in this equation, while Carbone & Bragg (2020) considered a definition of mean energy flux approximated based on solenoidal filtered velocity increments, and examined its connections to average vortex and strain stretching rates. Besides applications to isotropic homogeneous flow, numerous studies have investigated the application of the statistically averaged KH equation to spatially non-homogeneous flows. For instance, in wall-bounded flows, researchers have explored the energy cascade using a Reynolds decomposition to isolate effects of mean shear and non-homogeneity (Antonia *et al.* 2000; Danaila *et al.* 2001, 2012; Danaila, Anselmet & Zhou 2004; Marati *et al.* 2004; Cimarelli, De Angelis & Casciola 2013). Investigations have also studied the energy cascade rates in boundary layer bypass transition (Yao, Mollicone & Papadakis 2022) and flow separation

980 A42-2

(Mollicone *et al.* 2018). Furthermore, specific attention has been given to the study of inverse cascade in wake flows (Gomes-Fernandes, Ganapathisubramani & Vassilicos 2015; Portela, Papadakis & Vassilicos 2017) and at turbulent/non-turbulent interfaces (Zhou & Vassilicos 2020; Cimarelli *et al.* 2021; Yao & Papadakis 2023).

The notion of transfer, or flux, of kinetic energy across length scales is of particular practical interest also in the context of large eddy simulations (LES). There, the rate of energy cascade is referred to commonly as the subgrid-scale (SGS) or subfilter-scale (SFS) rate of dissipation. It is defined as the contraction between the subgrid stress tensor and the filtered strain-rate tensor, and arises as a source term in the transport equation for SGS/SFS kinetic energy (Piomelli *et al.* 1991; Meneveau & Katz 2000). This quantity characterizes the energy transfers between the resolved scale and the residual scale within the inertial range, which is also a local property (Eyink & Aluie 2009). The SGS dissipation is highly intermittent (Cerutti & Meneveau 1998), and can be both positive and negative locally, but on average, energy is known to be transferred from large scales to the residual scales (forward cascade). There is a considerable literature on the subject, starting from the seminal papers by Lilly (1967), Leonard (1975) and Piomelli *et al.* (1991). Some reviews include Meneveau & Katz (2000), Meneveau (2010) and Moser, Haering & Yalla (2021).

Without averaging, it has been a common observation that the SGS/SFS dissipation can be negative, which has often been interpreted as indicative of local inverse cascading of kinetic energy, i.e. energy transfer from small to large scales of motion ('backscatter'; Piomelli *et al.* 1991). Borue & Orszag (1998) noted that the forward cascade occurs predominantly in regions characterized by strong straining, where the magnitude of negative skewness of the strain tensor and vortex stretching are large. Conversely, backscatter was observed in regions with strong rotation. The relationship between SGS dissipation and stress topology and stress–strain alignment geometry was discussed and measured based on three-dimensional (3-D) particle image velocimetry measurements by Tao, Katz & Meneveau (2002). In a more recent study, Ballouz & Ouellette (2018) investigated the SGS tensor by considering the relative alignment of the filtered shear stress and strain tensors. They found that the energy cascade efficiency is quite low, a trend that they attributed to energy being transferred largely between positions in physical space. Quantitatively, in expressing the subgrid stress tensor as a superposition of all smaller-scale Gaussian-filtered velocity gradients, Johnson (2020, 2021) was able to isolate the relative contributions of small-scale strain self-stretching and vortex stretching, finding both to be important.

It has been questioned whether it is the local quantity $-\tau_{ij}\tilde{S}_{ij}$ (where τ_{ij} and $\tilde{S}_{ij}$ are the SGS stress and resolved strain-rate tensors, respectively) or the work done by the SGS/SFS force, $\tilde{u}_i\,\partial_j\tau_{ij}$ (where $\tilde{u}_i$ is the resolved velocity) that should be the genuine definition of local energy cascade rate. For instance, Kerr, Domaradzki & Barbier (1996) used the latter in their study of correlations of cascade rate and vorticity, and more recently Vela-Martín & Jiménez (2021) used both quantities in their analysis. Moreover, the SGS force plays a central role for optimal LES modelling (Langford & Moser 1999). The SGS force is invariant to divergence-free tensor fields, which therefore do not affect the large-scale dynamics, but certainly addition of such a tensor field to τ_{ij} can affect the usual definition of SGS dissipation $-\tau_{ij}\tilde{S}_{ij}$. By re-expressing the SGS stress and dissipation terms using an optimization procedure, Vela-Martín (2022) provided arguments that the often observed backscatter does not actually contribute to the energy cascade between scales but rather to the energy flux in the physical space, also suggesting that backscatter does not need to be modelled explicitly in LES.

As can be seen from this partial summary of the literature on backscatter and inverse cascade in the LES filtering approach, no consensus has been reached regarding the possible importance and physical interpretation of local backscatter using the definition based on the inner product of the subgrid stress and filtered strain-rate tensors. Also, the question of inverse cascade has not received much attention from the point of view of the local versions of the Kolmogorov equation in the structure-function approach. Therefore, in this paper we first revisit the generalized local structure-function formulation (§ 2.1). We argue that in this formulation, the term responsible for the energy cascade can be interpreted unambiguously as a flux of kinetic energy between scales since it appears inside a divergence in scale space. In this sense, it differs from the filtering formulation used in LES (reviewed in § 2.2) in which typically a fixed filter scale is used and no change in scales is considered, thus making the concept of a 'flux in scale space' less clearly defined and open to various interpretations.

With the definition of local cascade rate or energy flux clarified for the structure-function approach, we perform a comparative study of both the structure-function and filtering approaches' energy flux terms in a relatively high Reynolds number direct numerical simulation (DNS) database of forced isotropic turbulence at a Taylor-scale Reynolds number 1250. The data analysis is greatly facilitated by the availability of these data in a new version of the Johns Hopkins Turbulence Database (JHTDB) system, in which Python notebooks access the data directly (see Appendix A). The comparisons involve various statistical properties of the energy flux. First, in § 3 we provide comparisons of both quantities by means of simple statistical measures such as their mean values, joint probability density distributions and correlation coefficients, comparing both the two definitions of kinetic energy and kinetic energy cascade rate or flux. We then examine comparatively conditional averages based on the local molecular dissipation rate averaged over a ball of size ℓ, specifically re-examining the Kolmogorov refined similarity hypothesis (KRSH) in § 4. Then in § 5 we present comparative conditional averages of kinetic energy flux based on properties of the large-scale velocity gradient field such as the strain- and rotation-rate magnitudes, and the Q and R invariants. Particular attention is paid to events of local negative energy flux and whether or not such events can be considered to be of statistical significance. Overall conclusions are presented in § 6.

2. Local energy flux in the structure-function and filtering approaches

In this section, both the structure-function-based (KH equation) and filtering (LES) energy equations are reviewed. We focus on the term representing energy cascade (energy flux) in each equation, and describe some of the prior efforts in the literature relating the structure-function and filtering approaches.

2.1. *Energy cascade rate/flux in the scale-integrated local KH equation*

The KH equation is a generalized Kármán–Howarth equation that is derived directly from the incompressible Navier–Stokes equations without any modelling. Before averaging, the instantaneous KH equation with no mean flow and neglecting the forcing term reads (Hill 2001, 2002)

$$\frac{\partial \delta u_i^2}{\partial t} + u_j^* \frac{\partial \delta u_i^2}{\partial x_j} = -\frac{\partial \delta u_j \, \delta u_i^2}{\partial r_j} - \frac{8}{\rho} \frac{\partial p^* \, \delta u_i}{\partial r_i} + \nu \frac{1}{2} \frac{\partial^2 \delta u_i^2}{\partial x_j \, \partial x_j} + 2\nu \frac{\partial^2 \delta u_i^2}{\partial r_j \, \partial r_j} - 4\epsilon^*, \quad (2.1)$$

980 A42-4

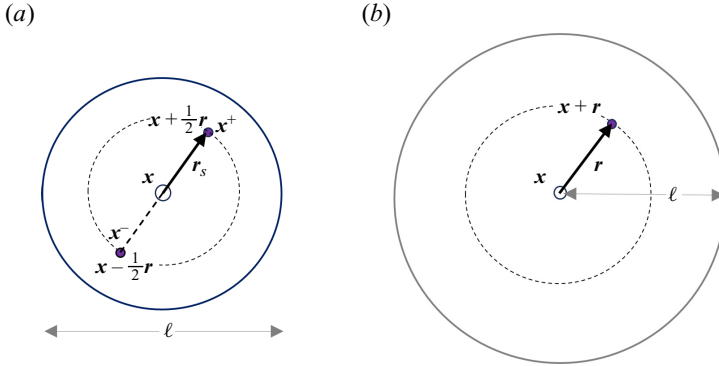(*a*)   (*b*)

Figure 1. (*a*) Sketch showing local domain of integration over a ball of diameter ℓ used in the symmetric Hill (2002) structure-function approach in which pairs of points separated by distances $r = 2r_s$ up to ℓ are used. (*b*) Integration up to a ball of radius ℓ in which pairs of points separated by distances r up to ℓ are used as in the approach of Duchon & Robert (2000). For volume averaging, in (*a*) 3-D integration over the vector r_s is performed at fixed x, while in (*b*) 3-D integration over the vector r is performed at fixed x. For surface integrations, in (*a*) integration is done over the spherical surface of radius $\ell/2$, while in (*b*) it is done over a spherical surface of radius ℓ.

where $\delta u_i = \delta u_i(x, r) = u_i^+ - u_i^-$ is the velocity increment vector in the *i*th Cartesian direction over displacement vector r. The superscripts $+$ and $-$ represent two points, $x + r/2$ and $x - r/2$, in the physical domain that have a separation vector $r_i = x_i^+ - x_i^-$ and middle point $x_i = (x_i^+ + x_i^-)/2$ (see figure 1*a*). The superscript $*$ denotes the average value between two points, e.g. the two-point average dissipation is defined as $\epsilon^*(x, r) = (\epsilon^+ + \epsilon^-)/2$, and $\epsilon^\pm$ here is the 'pseudo-dissipation' defined at every point as $\epsilon = \nu(\partial u_i/\partial x_j)^2$. (In Hill (2002), an alternate expression involving the real dissipation was introduced – his (2.13) – at the cost of including an additional pressure term.) Note that throughout this paper, when referring to 'dissipation' we will mean the pseudo-dissipation. Also, we will use $r_s = r/2$ to denote the radial coordinate vector from the local 'origin' x.

As remarked by Hill (2001, 2002), it is then instructive to apply integration over a sphere in r_s-space up to a radius $\ell/2$, i.e. over a sphere of diameter ℓ. The resulting equation is divided by the sphere volume $V_\ell = \frac{4}{3}\pi(\ell/2)^3$ and a factor 4, and Gauss' theorem is used for the r-divergence terms (recalling that $\partial r = 2\,\partial r_s$), yielding

$$
\begin{aligned}
\frac{1}{2V_\ell} &\iiint_{V_\ell} \left(\frac{\partial \delta u_i^2/2}{\partial t} + u_j^* \frac{\partial \delta u_i^2/2}{\partial x_j} \right) \mathrm{d}^3 r_s \\
&= -\frac{3}{4\ell} \frac{1}{S_\ell} \oint_{S_\ell} \delta u_i^2 \, \delta u_j \, \hat{n}_j \, \mathrm{d}S - \frac{6}{\rho\ell} \frac{1}{S_\ell} \oint_{S_\ell} p^* \, \delta u_j \, \hat{n}_j \, \mathrm{d}S \\
&\quad + \frac{\nu}{4} \frac{1}{V_\ell} \iiint_{V_\ell} \left(\frac{1}{2} \frac{\partial^2 \delta u_i^2}{\partial x_j \, \partial x_j} + 2 \frac{\partial^2 \delta u_i^2}{\partial r_j \, \partial r_j} \right) \mathrm{d}^3 r_s - \frac{1}{V_\ell} \iiint_{V_\ell} \epsilon^* \, \mathrm{d}^3 r_s,
\end{aligned} \tag{2.2}
$$

where S_ℓ represents the bounding sphere's surface of area $S_\ell = 4\pi(\ell/2)^2$, and $\hat{n}_j$ is the radial unit vector normal to the sphere surface. Equation (2.2) suggests defining a

structure-function-based kinetic energy at scale ℓ according to

$$k_{sf,\ell}(\boldsymbol{x}, t) = \frac{1}{2V_\ell} \iiint\limits_{V_\ell} \frac{1}{2} \delta u_i^2(\boldsymbol{x}, \boldsymbol{r}) \, \mathrm{d}^3 \boldsymbol{r}_s, \tag{2.3}$$

so that the first term in (2.2) corresponds to $\partial k_{sf,\ell}/\partial t$. The $1/2$ factor in front of the integral is justified since the volume integration over the entire sphere will double count the energy contained in $\delta u_i^2 = (u_i^+ - u_i^-)^2$. Equation (2.2) thus describes the transport of two-point, structure-function energy $k_{sf,\ell}$, which represents energy within eddies with length scales up to ℓ (Davidson 2015) in both the length scale ℓ and physical position $\boldsymbol{x}$ spaces. The last term in (2.2) represents the r-averaged rate of dissipation, with the radius vector $\boldsymbol{r}_s = \boldsymbol{r}/2$ being integrated up to magnitude $\ell/2$:

$$\epsilon_\ell(\boldsymbol{x}, t) \equiv \frac{1}{V_\ell} \iiint\limits_{V_\ell} \epsilon^*(\boldsymbol{x}, \boldsymbol{r}) \, \mathrm{d}^3 \boldsymbol{r}_s. \tag{2.4}$$

As remarked by Hill (2001, 2002), this quantity corresponds directly to the spherical average of local dissipation at scale ℓ, and plays a central role in the celebrated KRSH (Kolmogorov 1962).

The local energy cascade rate in the inertial range at position $\boldsymbol{x}$ and time t is defined as

$$\Phi_\ell(\boldsymbol{x}, t) \equiv -\frac{3}{4\ell} \frac{1}{S_\ell} \oint_{S_\ell} \delta u_i^2 \, \delta u_j \, \hat{n}_j \, \mathrm{d}S = -\frac{3}{4\ell} [\delta u_i^2 \, \delta u_j \, \hat{n}_j]_{S_\ell}, \tag{2.5}$$

where $[\cdot]_{S_\ell}$ indicates area averaging over the sphere of diameter ℓ. We note that in this definition, $\Phi_\ell(\boldsymbol{x}, t)$ represents the surface average of a flux that is defined positive if energy is flowing into the sphere in the r-scale space. The position is fixed at $\boldsymbol{x}$, thus the quantity $\Phi_\ell(\boldsymbol{x}, t)$ does not contain possible confounding spatial transport effects.

In terms of the overall average of (2.2), under the assumptions of homogeneous isotropic flow and statistical steady-state conditions, and for ℓ in the inertial range of turbulence, the unsteady transport and viscous terms vanish. The pressure term is also zero due to isotropy and incompressibility. Therefore, (2.2) can be simplified and yields, as expected,

$$\langle \Phi_\ell \rangle = \langle \epsilon_\ell \rangle = \langle \epsilon \rangle, \tag{2.6}$$

or equivalently, $[\delta u_i^2 \, \delta u_j \, \hat{n}_j]_{S_\ell} = -(4/3)\ell\langle \epsilon \rangle$, the $4/3$ law (Frisch 1995).

In this paper, the focus will be mainly on the flux term Φ_ℓ, with some attention also on the dissipation term ϵ_ℓ. Analysis of the time derivative, spatial advection terms and pressure terms is left for other ongoing studies. The viscous flux terms (in both spatial and scale spaces) are also not considered, since our present interest concerns the inertial range.

2.2. *Energy cascade rate/flux in the filtering approach*

In this subsection, we review the transport equation of the SGS kinetic energy (Germano 1992) for $k_{sgs,\ell} \equiv \frac{1}{2}\tau_{ii}$, where $\tau_{ij} = \widetilde{u_i u_j} - \tilde{u}_i \tilde{u}_j$ is the SGS stress tensor, with the tilde symbol ($\sim$) denoting spatial filtering of variables. The transport equation for $k_{sgs,\ell}$ reads

(Germano 1992)

$$\frac{\partial k_{sgs,\ell}}{\partial t} + \tilde{u}_j \frac{\partial k_{sgs,\ell}}{\partial x_j} = -\frac{1}{2} \frac{\partial}{\partial x_j} \left(\widetilde{u_i u_i u_j} - 2\tilde{u}_i \widetilde{u_i u_j} - \tilde{u}_j \widetilde{u_i u_i} - \tilde{u}_i \tilde{u}_i \tilde{u}_j \right) - \frac{\partial}{\partial x_j} \left(\widetilde{p u_j} - \tilde{p} \tilde{u}_j \right)$$

$$+ \frac{\partial}{\partial x_j} \left(\nu \frac{\partial k_{sgs,\ell}}{\partial x_j} \right) + \nu \frac{\partial \tilde{u}_i}{\partial x_j} \frac{\partial \tilde{u}_i}{\partial x_j} - \nu \widetilde{\frac{\partial u_i}{\partial x_j} \frac{\partial u_i}{\partial x_j}} - \tau_{ij} \tilde{S}_{ij}. \tag{2.7}$$

The last term is called the SGS rate of dissipation at position (x), and is often denoted as

$$\Pi_\ell(x, t) \equiv -\tau_{ij} \tilde{S}_{ij}. \tag{2.8}$$

For filtering, in the present work, we consider a spherical-shaped sharp top-hat filter in physical space with diameter ℓ. Therefore, for any field variable $A(x)$, we define the filtered variable as $\tilde{A}(x) = V_\ell^{-1} \iiint_{V_\ell} A(x + r_s) \, \mathrm{d}^3 r_s$. Note that each term in (2.2) and (2.7) is thus evaluated at the same length scale. Terms in (2.7) can be compared directly to terms in (2.2); in particular, the local dissipation terms are exactly the same, i.e.

$$-\nu \widetilde{\frac{\partial u_i}{\partial x_j} \frac{\partial u_i}{\partial x_j}} = -\frac{1}{V_\ell} \iiint_{V_\ell} \nu \frac{\partial u_i}{\partial x_j} \frac{\partial u_i}{\partial x_j} \, \mathrm{d}^3 r_s = \epsilon_\ell(x, t). \tag{2.9}$$

Again, for homogeneous steady-state turbulence in the inertial range (neglecting viscous diffusion and resolved dissipation terms), upon averaging, (2.7) simplifies to

$$\langle \Pi_\ell \rangle = \langle \epsilon_\ell \rangle = \langle \epsilon \rangle, \tag{2.10}$$

which is similar to (2.6); thus on average, certainly the two definitions of energy cascade rate/flux agree with each other, i.e. $\langle \Pi_\ell \rangle = \langle \Phi_\ell \rangle$.

It is also of interest to compare the average value of the two definitions of kinetic energy used in both definitions of energy cascade rate/flux. In the inertial range of high Reynolds number turbulence, both $\langle k_{sf,\ell} \rangle$ and $\langle k_{sgs,\ell} \rangle$ can be evaluated based on the Kolmogorov $r^{2/3}$ law and $k^{-5/3}$ spectrum, respectively. The result is (see Appendix B for details) $\langle k_{sf,\ell} \rangle \approx 1.6 \langle \epsilon \rangle^{2/3} \ell^{2/3}$ and $\langle k_{sgs,\ell} \rangle \approx 1.2 \langle \epsilon \rangle^{2/3} \ell^{2/3}$. In other words, they are of similar order of magnitude but the SGS kinetic energy is slightly smaller.

2.3. *Other relationships between the structure-function and filtering approaches*

In the present paper, we will perform the data analysis and comparisons using the two approaches mentioned above (scale-integrated local KH and filtering formulations). However, it is useful at this stage to include some remarks regarding other structure-function and energy definitions used in earlier works by Vreman, Geurts & Kuerten (1994), Constantin, Weinan E & Titi (1994), Duchon & Robert (2000), Eyink (2002) and Dubrulle (2019). Those approaches focus typically on the structure function written at one of the endpoints instead of the midpoint. Duchon & Robert (2000) and Dubrulle (2019) focus on the two-point correlation quantity $C(x, r) = u_i(x) \, u_i(x + r)$ (see figure 1b). Local averaging over all values of r from $r = 0$ up to scale $|r| = \ell$ at any given x then corresponds to the 'mixed' energy quantity $u_i \tilde{u}_i / 2$ (denoted as E^ℓ in Dubrulle 2019), where the filtering is over a sphere of diameter 2ℓ so as to combine two points with separation distances up to ℓ. The quantity $C(x, r)$ combines filtered and unfiltered velocities, hence it is more difficult to interpret for comparisons of structure-function and

LES filtering approaches. In their transport equation, Duchon & Robert (2000) show that a term similar to the third-order structure-function term of (2.5) arises. However, in order for the structure function to correspond to scale ℓ, one has to choose to integrate over a sphere of diameter 2ℓ (the locally integrated dissipation rate would then be $\epsilon_{2\ell}$). In a spherical integration over r of powers of the velocity difference $[u_i(x+r) - u_i(x)]$, only the first term is affected by filtering or averaging over the spherical shell, while the centre velocity $u_i(x)$ remains fully local. Note that in the scale-integrated local KH equation, the averaging affects both endpoint velocities in the same way, and both become averaged at scale ℓ in a formally symmetric way.

An early connection between structure-function and filtering approaches was developed by Vreman *et al.* (1994). In the Vreman analysis, the structure function is defined based on the difference of velocity $u_i(x+r)$ and the locally filtered velocity $\tilde{u}_i$ centred at x. Spherical integration of $(u_i(x+r) - \tilde{u}_i)^2$ over a sphere of radius $\ell/2$ then yields equivalence with the SGS kinetic energy at scale ℓ. But $(u_i(x+r) - \tilde{u}_i)^2$ does not equal the usual structure-function definition, now due to a mixture of filtered and unfiltered quantities at two points even before local filtering.

Another interesting approach was presented in Constantin *et al.* (1994) and connected to the LES filtering approach by Eyink (1995, 2006) (equations (2.12)–(2.14) in the latter). In fact, as recounted in the review by Eyink & Sreenivasan (2006), early unpublished work by Onsager anticipated such expressions half a century prior. Written in terms of the sharp spherical filter that we use here, the expression for the trace of the SGS stress reads

$$\tau_{ii}(x) = \frac{1}{V_\ell} \iiint_{V_\ell} [u_i(x+r) - u_i(x)]^2 \, \mathrm{d}^3r - \left(\frac{1}{V_\ell} \iiint_{V_\ell} [u_i(x+r) - u_i(x)] \, \mathrm{d}^3r \right)^2.$$

(2.11)

This equation represents an exact relationship between two-point structure functions and the SGS kinetic energy. But for the right-hand side to correspond to structure functions up to scale ℓ, the integration must be done over a sphere of radius ℓ and thus a filtering scale of 2ℓ for the stress tensor in the filtering formulation. The suggested relationship then appears to be between SGS stress kinetic energy at scale 2ℓ and structure functions up to two-point separations ℓ but averaged over a local domain of size 2ℓ, similarly to the Duchon & Robert (2000) approach. Note that while each of the terms in (2.11) is also a mixture of filtered and unfiltered velocities, the subtraction cancels the local term and restores the fully filtered property inherent in the definition of τ_{ii}.

While not expecting qualitatively different results (except perhaps using the diameter instead of the radius as a name for 'scale'), we here continue our focus on the more 'symmetric' formulation by Hill, with fixed position x specified at the midpoint between two points separated by vector r whose magnitude then spans up to scale ℓ (or integration radius r_s up to radius $\ell/2$).

3. Comparisons between kinetic energies and cascade rates/fluxes

In this section, we provide comparisons of local kinetic energies in the structure-function formalism, $k_{sf,\ell}$, with that in the filtering formalism, $k_{sgs,\ell}$. We also compare the local energy cascade rates Φ_ℓ and Π_ℓ. We consider data from DNS of forced isotropic turbulence at $R_\lambda = 1250$ (the Taylor-scale Reynolds number) that used 8192^3 grid points (Yeung, Donzis & Sreenivasan 2012) in a computational domain of size $(2\pi)^3$.

The integral scale of the flow is $L = 1.24$, the velocity root mean square is $u' = 1.58$, and the mean dissipation is $\langle \epsilon \rangle = 1.36$. More details about the data and simulation parameters are available as supplementary material at https://doi.org/10.1017/jfm.2023.1066. The analysis is performed at four length scales in the inertial range $\ell = \{30, 45, 60, 75\}\eta$, where $\eta = (\nu^3/\langle \epsilon \rangle)^{1/4}$ is the Kolmogorov length scale, the value of which is 4.98×10^{-4}. Comparing to the transverse Taylor microscale (Pope 2000) $\lambda_g = u'(15\nu/2\langle \epsilon \rangle)^{1/2} \approx 0.024$, the four length scales are $\ell = \{0.62, 0.93, 1.24, 1.55\}\lambda_g$, respectively.

To compute volume spherically filtered quantities such as $k_{sgs,\ell}$ and τ_{ij} (and filtered velocity gradient tensor, to be discussed in § 5), we fix the middle point coordinate $\boldsymbol{x}$ in the physical domain. Subsequently, we download data in a cubic domain using the JHTDB cutout service in a cube of size ℓ^3. The data are then multiplied by a spherical mask (filter) to evaluate local filtered quantities. Other quantities are obtained by utilizing pre-computed Getfunctions from the JHTDB, including spatial interpolation and differentiation, as explained in more detail in Appendix A. For surface averages such as Φ_ℓ, we discretize the outer surface of diameter ℓ into 500 points (for the largest $\ell/\eta = 75$ case, 2000 points are used) that are distributed approximately uniformly on the sphere. The accuracy of this method of integration has been tested for the $\ell/\eta = 45$ case by comparing the results from using 500 points to those using 2000 points, for a smaller testing subsample of 500 randomly chosen spheres. We verified that the difference between the mean values of Φ_ℓ, as well as the average of the absolute value of differences, was less than 1 %. For volume averages such as ϵ_ℓ and $k_{sf,\ell}$, we use 5 shells for $\ell/\eta = 30, 45, 60$. The outermost shell comprises 500 uniformly distributed points, with a reduction in number of points towards the inner shells, approximately maintaining the density. We tested 500 randomly chosen spheres to calculate ϵ_ℓ at $\ell/\eta = 45$ using 5 shells and 10 shells. The difference between the mean values of ϵ_ℓ, as well as the average of the absolute value of differences, was less than 2 %. For the larger length scale $\ell/\eta = 75$, the number of shells was increased to 6; the accuracy is tested using the same method as employed for $\ell/\eta = 45$. For all the calculations, data on the specified points are obtained from the database using eighth-order Lagrange spatial interpolation. We tested different spatial interpolation methods even without interpolation (using the closest grid point values), verifying that essentially, the averaged values of interest were unchanged.

Overall mean values are obtained at the four scales and are plotted in figure 2(*a*). The results for kinetic energy for the structure-function approach are consistent with the analytical evaluation (see Appendix B). For the SGS kinetic energy, the numerical results fall below the theoretical inertial range prediction, due to the transfer function of top-hat filtering having a very different spectral signature compared to the structure function, and when integrating, it emphasizes the viscous range more than the structure-function operation, reducing the amount of SGS kinetic energy even at scales much larger than the Kolmogorov scale (see discussion in Appendix B).

Figure 3(*a*) shows the joint probability density function (p.d.f.) of $k_{sf,\ell}$ and $k_{sgs,\ell}$ at scale $\ell = 45\eta$. The correlation coefficient between the quantities is $\rho_{kk} = 0.97$ (figure 2*b*). The correlation coefficient is defined as $\rho_{xy} = \langle (x - \langle x \rangle)(y - \langle y \rangle) \rangle / (\sigma_x \sigma_y)$, where σ represents the variable's root mean square value. Similarly, figure 3(*b*) shows the joint p.d.f. of Π_ℓ and Φ_ℓ, also at scale $\ell = 45\eta$ for the same dataset. The correlation coefficient between the quantities is measured to be $\rho_{\Phi\Pi} = 0.58$ (figure 2*b*), significantly lower than for the energies but still appreciable. It can be seen that negative values occur for both Π_ℓ and Φ_ℓ, although it appears that Φ_ℓ has more variability and larger negative excursions
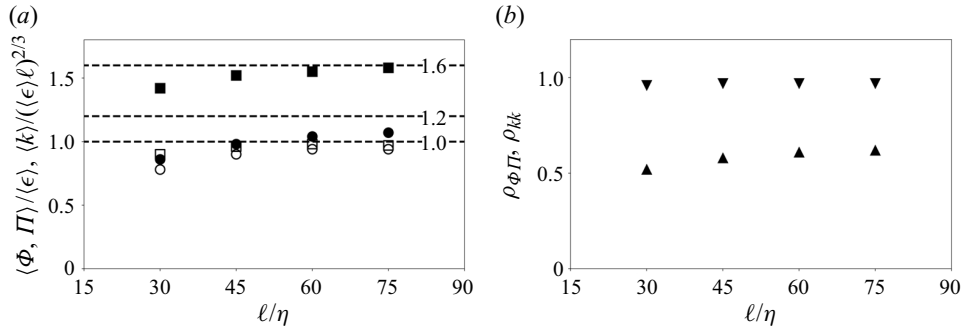
Figure 2. (*a*) Normalized mean kinetic energies and mean cascade rates as functions of four filter scales for the $R_\lambda = 1250$ DNS isotropic turbulence dataset. Specifically, closed squares show $\langle k_{sf,\ell} \rangle / (\langle \epsilon \rangle \ell)^{2/3}$ while closed circles show $\langle k_{sgs,\ell} \rangle / (\langle \epsilon \rangle \ell)^{2/3}$. Open squares show $\langle \Phi_\ell \rangle / \langle \epsilon \rangle$, while open circles show $\langle \Pi_\ell \rangle / \langle \epsilon \rangle$. The horizontal lines show the expected asymptotic values in the inertial range for mean kinetic energies in the structure-function formulation (1.6) and in the filtering formulation (1.2), while the expected energy cascade rates equal unity. (*b*) The correlation coefficients between kinetic energies (ρ_{kk}, downward triangles) and cascade rates ($\rho_{\Phi \Pi}$, upward triangles).
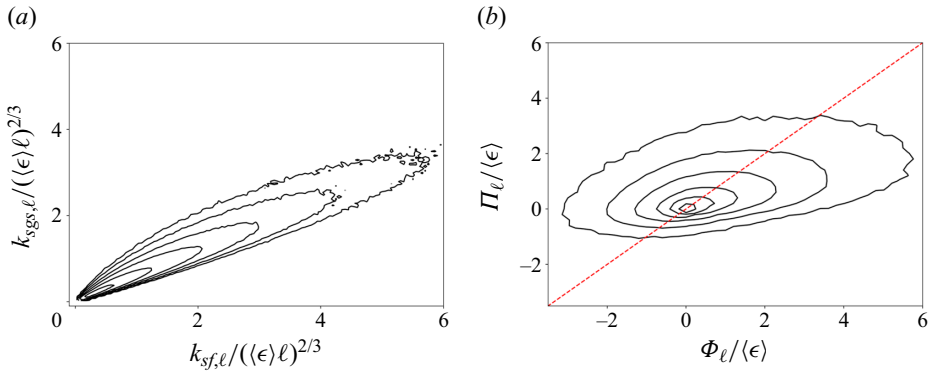

Figure 3. Joint p.d.f.s of (*a*) $k_{sgs,\ell}$ and $k_{sf,\ell}$ with contour line values 0.01, 0.03, 0.1, 0.3, 1, 3, and (*b*) Π_ℓ and Φ_ℓ with contour line values 0.001, 0.003, 0.01, 0.3, 0.1, 0.3, at scale $\ell = 45\eta$ measured in DNS of isotropic turbulence at $R_\lambda = 1250$. The red dashed line represents a 45-degree slope line. The data and the editable notebook can be found at https://www.cambridge.org/S0022112023010662/JFM-Notebooks/files/figure3.

than Π_ℓ. As summarized in §1, the relevance of locally negative values of Π_ℓ to the flow physics remains unclear, especially given the fact that upon averaging, the quantity becomes positive. Conversely, the quantity Φ_ℓ has a clearer local interpretation, in the sense that clearly, locally negative values can be interpreted as kinetic energy (local $\delta u_i^2/2$)) showing a net flux out of a sphere of diameter ℓ in scale space, i.e. becoming associated with energy at larger ℓ, while its overall average is positive. An interesting question is whether negative values of Π_ℓ or Φ_ℓ survive under some type of statistical averaging. In the following sections, we use conditional averaging to quantify the importance of negative values (inverse local cascade, or backscatter).

4. Conditional averaging based on local dissipation

Motivated by the KRSH and the fact that local viscous dissipation (small-scale) appears in both the scale-integrated local KH equation and the SGS kinetic energy equation (i.e. (2.4) is identical to (2.9)), in this section, we compare conditionally averaged cascade rates/fluxes for both the structure-function and filtering formulations, conditioned on ϵ_ℓ,
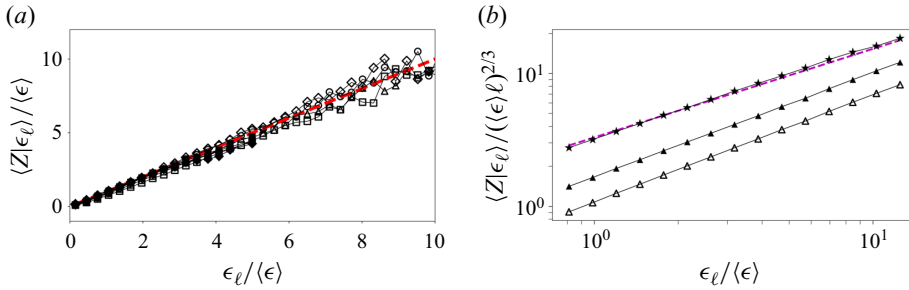
980 A42-10

Figure 4. (*a*) Conditional averages of $Z = \Phi_\ell$ (black symbols and lines) and $Z = \Pi_\ell$ (open symbols and lines) based on local dissipation ϵ_ℓ. The red dashed line indicates the value of ϵ_ℓ. Different symbols denote different scales: $\ell/\eta = 30$ (squares), 45 (triangles), 60 (circles) and 75 (diamonds). All values are normalized with the globally averaged rate of dissipation $\langle\epsilon\rangle$. (*b*) Log-log plot of conditional averages of $Z = k_{sf,\ell}$ (black triangles) and $Z = k_{sgs,\ell}$ (open triangles) based on local dissipation ϵ_ℓ for the case $\ell = 45\eta$. Black stars show the conditional average of the longitudinal velocity increments $Z = \delta u_L^2$, where $\delta u_L = \delta u_j \hat{n}_j$. The magenta dashed line has slope 2/3 according to Kolmogorov theory.

i.e. $\langle\Phi_\ell|\epsilon_\ell\rangle$ and $\langle\Pi_\ell|\epsilon_\ell\rangle$. According to the KRSH (Kolmogorov 1962), the statistical properties of velocity increments depend on the local average dissipation within a sphere of scale ℓ, rather than being determined by the globally averaged dissipation. Written in terms of the quantities of present interest, the KRSH would read $\langle\Phi_\ell|\epsilon_\ell\rangle = \epsilon_\ell$ since Φ_ℓ is determined fully by the velocity increments envisioned in the KRSH. Loosely extending the KRSH arguments to the filtering formalism would suggest $\langle\Pi_\ell|\epsilon_\ell\rangle = \epsilon_\ell$.

In order to assess this hypothesis, we evaluate the conditional averages based on the same dataset as described before. Results for $\langle\Phi_\ell|\epsilon_\ell\rangle$ and $\langle\Pi_\ell|\epsilon_\ell\rangle$ are shown in figure 4(*a*). Results for the four scales considered are included. As can be seen, the plot shows close agreement for both $\langle\Phi_\ell|\epsilon_\ell\rangle$ and $\langle\Pi_\ell|\epsilon_\ell\rangle$ with ϵ_ℓ. It is important to note that Φ_ℓ and Π_ℓ are conditioned on exactly the same values of ϵ_ℓ. The similarities and differences observed in figure 4 indicate that Φ_ℓ and Π_ℓ share many properties (same conditional averages) but they are not identical. For instance, it is clear from figure 3(*b*) that the variance of Φ_ℓ exceeds that of Π_ℓ, even though their mean values are the same.

In general, the behaviours of both $\langle\Phi_\ell|\epsilon_\ell\rangle$ and $\langle\Pi_\ell|\epsilon_\ell\rangle$ confirm the validity of the KRSH in the present context. More detailed analysis of the KRSH for Φ_ℓ and connections to (2.2) are reported in Yao *et al.* (2023). We also tested the KRSH using the full viscous dissipation $\nu(\partial u_i/\partial x_j)(\partial u_i/\partial x_j + \partial u_j/\partial x_i)$ instead of the pseudo-dissipation $\nu(\partial u_i/\partial x_j)^2$ when computing ϵ_ℓ. The largest difference for $\langle\Phi_\ell|\epsilon_\ell\rangle$ is less than 1 %. Additionally, the correlation coefficient between the two types of dissipation is 0.996.

Similarly, we evaluate the kinetic energies k_{sf} and k_{sgs} conditionally averaged on ϵ_ℓ. Results for k_{sf} and k_{sgs} are essentially indistinguishable, except for a constant offset consistent with the ratio of their mean values. In terms of their dependence on dissipation, we observe power-law scaling $\sim\epsilon_\ell^\beta$ with $\beta \sim 0.79$, slightly larger than the value 2/3 implied by standard Kolmogorov scaling. To verify the present data and analysis methods, we also evaluate the traditional longitudinal second-order structure function conditioned on ϵ_ℓ, $\langle\delta u_L^2|\epsilon_\ell\rangle$ (where $\delta u_L = \delta u_j \hat{n}_j$), for which the Kolmogorov scaling $\sim\epsilon_\ell^{2/3}$ according to the KRSH is well established (Stolovitzky, Kailasnath & Sreenivasan 1992). The result (shown as stars in figure 4*b*) indeed confirms the 2/3 scaling for this quantity. A more in-depth analysis and possible reasons for non-Kolmogorov scaling of k_{sf} with ϵ_ℓ are

left for future studies. At this stage, we simply note the similarity in scaling and overall behaviour of k_{sf} and k_{sgs}.

5. Conditional averaging based on large-scale velocity gradients

In this section, motivated by large-scale properties of the flow that would be available in LES, we explore correlations between properties of the velocity gradient tensor filtered at scale ℓ and the two definitions of energy cascade rate/flux. It is useful to cast the present comparative study of Φ and Π using analyses of the type that have been performed before in the context of LES. The velocity gradient tensor encapsulates information about fluid deformation and rotation, and connections to the energy cascade have been studied extensively. Already, Bardina, Ferziger & Rogallo (1985) examined the impact of rotation on homogeneous isotropic turbulence and observed that rotation decreases the dissipation (cascade) rate while increasing the length scales, suggestive of inverse energy cascade effects. Goto (2008) investigated physical mechanisms underlying forward energy cascade and argued that forward cascade can be triggered in regions characterized by strong strain between two large-scale tubular vortices. The role of the filtered gradient tensor for energy cascade was first explored numerically in Borue & Orszag (1998) and experimentally in van der Bos *et al.* (2002), building on the 'Clark model' that approximates features of the SGS tensor using Taylor-series expansion. Recent studies by Johnson (2020, 2021) and Carbone & Bragg (2020) have expanded significantly on such analyses, and examined the roles of strain-rate self amplification and vortex stretching driving the forward energy cascade process. For inverse cascade, a vortex thinning mechanism may be at play (Johnson 2021).

A first level of characterization of the properties of the velocity gradient tensor is its invariants. To characterize rates of deformation and rotation, we evaluate the strain and rotation invariants from data, defined according to

$$S_\ell^2(\boldsymbol{x}, t) = \tilde{S}_{ij}\tilde{S}_{ij}, \quad \Omega_\ell^2(\boldsymbol{x}, t) = \tilde{\Omega}_{ij}\tilde{\Omega}_{ij}, \tag{5.1a,b}$$

where S_{ij} and Ω_{ij} are the symmetric and antisymmetric parts of the velocity gradient tensor $A_{ij} = \partial u_i/\partial x_j$, and the tilde denotes, as before, spherical top-hat filtering over a ball of diameter ℓ. For consistency with prior literature, these values will be normalized by the overall average $\langle Q_w \rangle = \frac{1}{2}\langle \Omega_\ell^2 \rangle$ (equal to $\frac{1}{2}\langle S_\ell^2 \rangle$ in homogeneous turbulence).

A more detailed characterization of the statistics of velocity gradients involves the invariants Q and R (Vieillefosse 1982). It is well known that the joint p.d.f. of Q and R exhibits a characteristic teardrop shape (Chong, Perry & Cantwell 1990; Meneveau 2011), from which flow topology information such as vortex stretching and compression can be inferred (Chong *et al.* 1990; Borue & Orszag 1998; Lüthi, Holzner & Tsinober 2009; Danish & Meneveau 2018). These two invariants (at scale ℓ) are defined as usual according to

$$Q_\ell(\boldsymbol{x}, t) = -\tfrac{1}{2}\tilde{A}_{ij}\tilde{A}_{ji}, \quad R_\ell(\boldsymbol{x}, t) = -\tfrac{1}{3}\tilde{A}_{ij}\tilde{A}_{jk}\tilde{A}_{ki}. \tag{5.2a,b}$$

Under the assumption of restricted Euler dynamics (Meneveau 2011), the transport equation for the velocity gradient tensor leads to $\mathrm{d}Q_\ell/\mathrm{d}t = -3R_\ell$ and $\mathrm{d}R_\ell/\mathrm{d}t = -\tfrac{2}{3}Q_\ell^2$ (Cantwell 1992). The quantity R_ℓ can thus be considered as the (negative) rate of change of Q_ℓ, and contains both vortex stretching and strain self-stretching mechanisms (Johnson 2021). In our comparative investigation of energy cascade rates, conditional averaging based on the four invariant quantities S_ℓ^2, Ω_ℓ^2, Q_ℓ and R_ℓ will be undertaken.

We begin with qualitative visualizations of the fields in small subsets of the domains analysed. Figures 5(a,b) depict sample instantaneous fields of Φ_ℓ and Π_ℓ, respectively,
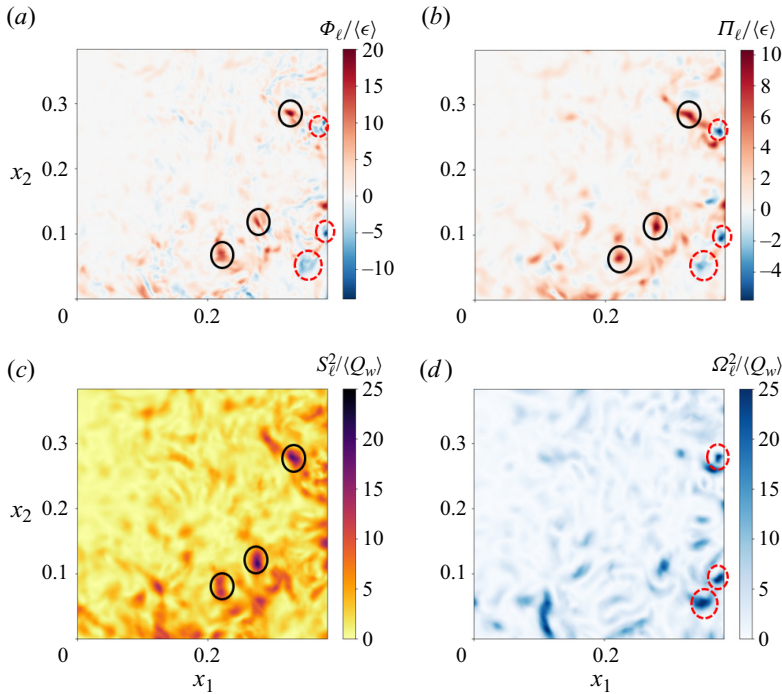
Figure 5. (*a–d*) Instantaneous Φ_ℓ, Π_ℓ, S_ℓ^2 and Ω_ℓ^2 fields, respectively, with $\ell = 45\eta$ in a $750\eta \times 750\eta$ domain (500×500 points of the DNS grid). The black solid circles in (*a,b*) are located in the strong local forward cascade region, which is correlated to the strong local strain rates marked in the black circles in (*c*). The red dashed circles in (*a,b*) are located in local inverse cascade regions (negative energy fluxes), which appear correlated qualitatively to relatively strong local rotation rates marked in the red dashed circles in (*d*).

highlighting regions of strong local forward cascade (indicated by solid black circles) and strong inverse cascade (indicated by dashed red circles). The correlation between these two variables is evident; the computed correlation coefficient between the snapshots is 0.64. In both figures 5(*a,b*), the fluxes are normalized by the global averaged dissipation $\langle\epsilon\rangle$. As already noted based on the joint p.d.f.s, there are differences between Φ_ℓ and Π_ℓ. The maximum magnitude of the positive cascade rate in Φ_ℓ is approximately twice that of Π_ℓ, while the magnitude of the negative cascade rate in Φ_ℓ is approximately 3–4 times larger. Since $\langle\Phi_\ell\rangle \sim \langle\Pi_\ell\rangle \sim \langle\epsilon_\ell\rangle \sim \langle\epsilon\rangle$, the significant different maximum values indicate that Φ_ℓ is more variable and intermittent than Π_ℓ. Also, Φ_ℓ exhibits somewhat finer-scale spatial features.

5.1. *Conditional statistics based on strain rate (S_ℓ^2) and rotation rate (Ω_ℓ^2)*

Figures 5(*a,b*) show distinct regions including both local forward (red area) and inverse (blue area) cascade rates. It is apparent visually that the presence of a strong local forward energy cascade is associated with increased local strain rate, as indicated by the solid black circles in both figures 5(*a,b*) and the corresponding black solid circles in figure 5(*c*). Similarly, a strong local inverse energy cascade is observed alongside a significant local rotation rate, depicted by the dashed red circles in figures 5(*a,b*) and the corresponding red dashed circles in figure 5(*d*). The strong correlation between forward cascade and local straining is consistent with multiple earlier observations and prior works in the literature
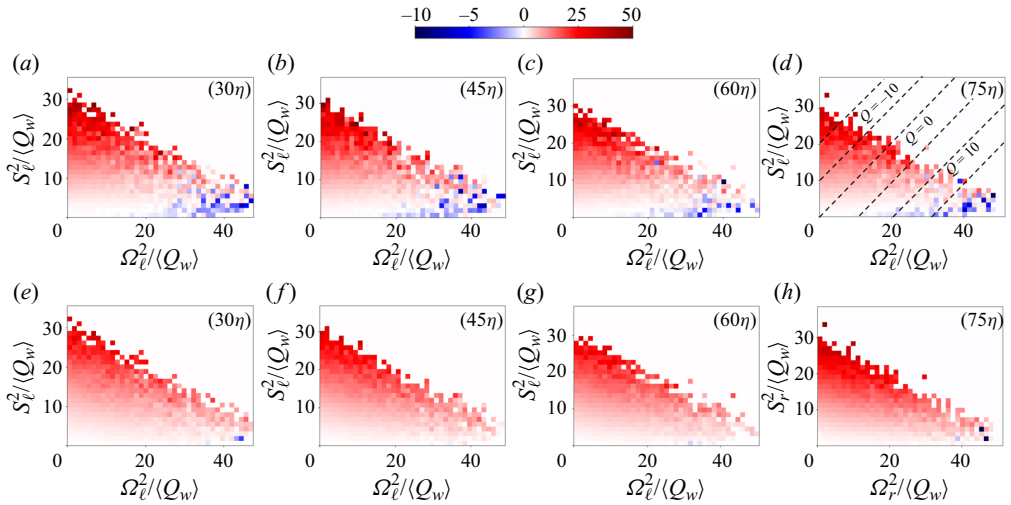
Figure 6. Plots of (*a–d*) $\langle \Phi_\ell | S_\ell^2, \Omega_\ell^2 \rangle$ and (*e–h*) $\langle \Pi_\ell | S_\ell^2, \Omega_\ell^2 \rangle$ at $\ell = \{30, 45, 60, 75\}\eta$. The black dashed lines in (*d*) represent isolines of $Q_\ell \equiv -\frac{1}{2}(S_\ell^2 - \Omega_\ell^2)$; Φ_ℓ and Π_ℓ is normalized by $\langle \epsilon \rangle$; and S_ℓ^2 and Ω_ℓ^2 is normalized by $\langle Q_w \rangle = \frac{1}{2}\langle \Omega_\ell^2 \rangle$.

(e.g. Borue & Orszag 1998, and recently Johnson 2021; Carbone & Bragg 2020). We focus attention on the regions with negative energy cascade rates. Conditional averaging can elucidate the statistical significance of these regions. Specifically, we inquire whether there are large-scale flow local features as characterized by the filtered velocity gradient invariants that are systematically accompanied by inverse cascade, i.e. negative Φ_ℓ. Thus we perform conditional averaging of Φ_ℓ based on the invariants S_ℓ^2 and Ω_ℓ^2, and repeat the analysis for the SGS energy flux quantity Π_ℓ.

Figure 6 shows the joint conditionally averaged Φ_ℓ and Π_ℓ based on S_ℓ^2 and Ω_ℓ^2, denoted as $\langle \Phi_\ell | S_\ell^2, \Omega_\ell^2 \rangle$ and $\langle \Pi_\ell | S_\ell^2, \Omega_\ell^2 \rangle$, respectively. The analysis is performed by computing averages over two million randomly distributed points x. In the presented results, Φ_ℓ is normalized by $\langle \epsilon \rangle$, while S_ℓ^2 and Ω_ℓ^2 are normalized by $\langle Q_w \rangle = \frac{1}{2}\langle \Omega_\ell^2 \rangle$. Figures 6(*a–d*) present the joint conditionally averaged $\langle \Phi_\ell | S_\ell^2, \Omega_\ell^2 \rangle$ at four different length scales, namely $\ell = \{30, 45, 60, 75\}\eta$, highlighting the dominance of the forward cascade by the extensive red region. This magnitude is many times larger than the maximum magnitude observed in the blue region, representing the inverse cascade. The red region covers a wide range of S_ℓ^2 and Ω_ℓ^2 values, consistent with the expectation that the global average would favour a forward cascade ($\langle \Phi_\ell > 0 \rangle$). The highest positive values of $\langle \Phi_\ell | S_\ell^2, \Omega_\ell^2 \rangle$ correspond to high strain rates and low rotation rates, and they decrease as the strain rate decreases. Interestingly, the inverse cascade appears explicitly in the lower-right corners of the plots, where the rotation rate is strong but the strain rate is weak. It is worth noting that the conditionally averaged values shown in figure 6 reflect the combined outcome of the forward and inverse cascades. Consequently, in specific regions characterized by distinct strain and rotation rates, events with forward and inverse cascades can cancel each other out. Only in the lower right corner is there an indication of net inverse cascade when the cascade rate is defined using the structure-function approach.

In figure 6(*d*), we superimpose dashed lines representing the isolines of Q_ℓ, with the $Q_\ell = 0$ line indicating the condition of equal strain and rotation rates. The parallel dashed lines correspond to $Q_\ell = -10, -5, 0, 5, 10$ and 15, respectively. The $Q_\ell = 15$ line appears
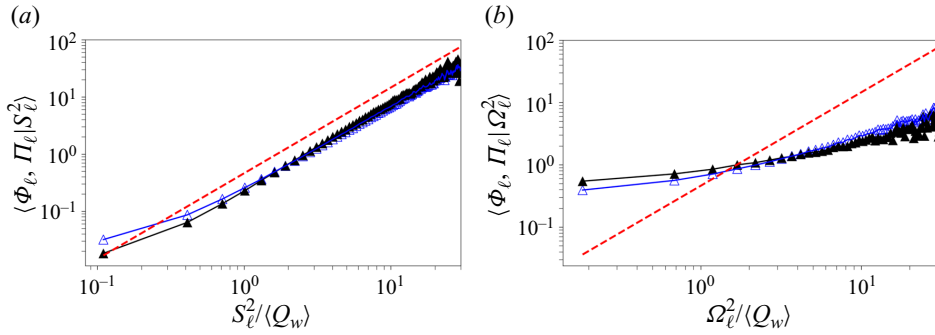
Figure 7. (*a*) Plots of $\langle \Phi_\ell | S_\ell^2 \rangle$ (black triangles and lines) and $\langle \Pi_\ell | S_\ell^2 \rangle$ (blue open triangles and lines). (*b*) Plots of $\langle \Phi_\ell | \Omega_\ell^2 \rangle$ (black triangles and lines) and $\langle \Pi_\ell | \Omega_\ell^2 \rangle$ (blue open triangles and lines). The red dashed lines represent lines with slope 3/2 in the log-log plot.

near the boundary separating the red and blue regions. However, the boundary of the blue region does not appear to align well with the Q_ℓ isoline. This observation suggests that Q_ℓ might be not enough to provide an adequate threshold for distinguishing the net forward and inverse cascade regions.

Figures 6(*d*–*g*) present results for the joint conditionally averaged Π_ℓ based on S_ℓ^2 and Ω_ℓ^2, corresponding to the same filter scales as in figures 6(*a*–*d*). It is evident that trends for the positive cascade rate (red region) for Π_ℓ resemble closely those of Φ_ℓ, with the peak of the forward cascade occurring at a high strain rate and low rotation rate. The magnitude of the maximum forward cascade rate for Π_ℓ is slightly weaker compared to that of Φ_ℓ. The most significant difference is that only a few instances of blue squares are observed in regions characterized by strong rotation and weak strain, indicating that the overall predominance of the forward cascade persists regardless of the local values of S_ℓ^2 and Ω_ℓ^2. These results highlight some important statistical differences between Φ_ℓ and Π_ℓ. We further evaluate the conditional averages of the energy fluxes Φ_ℓ and Π_ℓ, conditioned on either S_ℓ^2 and Ω_ℓ^2 individually. This analysis is motivated by the work of Buaria & Pumir (2022), which highlighted different scalings of conditional averages with respect to strain rate compared to rotation rates even though one would expect similar results based on dimensional arguments. In figure 7(*a*), we demonstrate that both Φ_ℓ and Π_ℓ exhibit a power-law relationship when conditioned on S_ℓ^2, with slope 3/2. This scaling aligns with dimensional analysis and Kolmogorov scaling, $\langle \Phi_\ell | S_\ell^2 \rangle \sim [S_\ell^2]^{3/2}$ and $\langle \Pi_\ell | S_\ell^2 \rangle \sim [S_\ell^2]^{3/2}$. In contrast, when conditioning Φ_ℓ and Π_ℓ on Ω_ℓ^2 (figure 7*b*), a different trend emerges, with much weaker dependence on rotation rate.

To develop a more detailed understanding of the inverse cascade region within $\langle \Phi_\ell | S_\ell^2, \Omega_\ell^2 \rangle$, we perform a further analysis by dividing the samples based on $\Phi_\ell > 0$ and $\Phi_\ell < 0$ for $\ell = 45\eta$. We then calculate the conditional average of these separated samples considering S_ℓ^2 and Ω_ℓ^2, denoted as $\langle \Phi_\ell | S_\ell^2, \Omega_\ell^2, \Phi_\ell > 0 \rangle$ and $\langle \Phi_\ell | S_\ell^2, \Omega_\ell^2, \Phi_\ell < 0 \rangle$. The results are presented in figure 8. From figure 8(*a*), it can be observed that the forward cascade clearly increases with S_ℓ^2, with the highest values of Φ_ℓ concentrated in the upper left corner. It increases also with Ω_ℓ^2, but less rapidly. Combined, the trend seems to be an increase approximately proportional to $\sim S_\ell^2 + 0.75\,\Omega_\ell^2$. Differently, figure 8(*b*) illustrates that the inverse cascade is approximately proportional to $\sim S_\ell^2 + 0.5\,\Omega_\ell^2$, i.e. shallower isolines extending more in the horizontal direction than in the vertical compared to the forward cascade case shown in figure 8(*a*). This observation elucidates why the
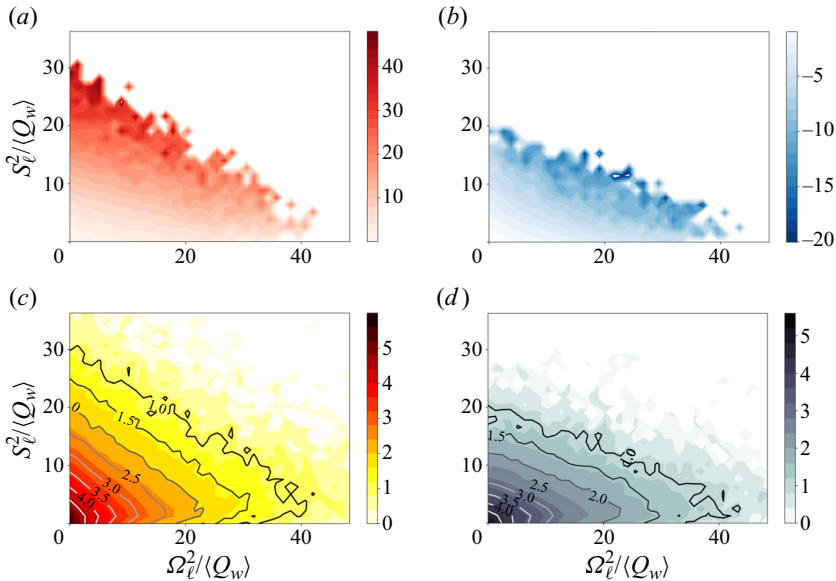
Figure 8. (*a,b*) The conditional averages of cascade rates obtained by sampling positive and negative signs, i.e. $\langle \Phi_\ell | S_\ell^2, \Omega_\ell^2, \Phi_\ell > 0 \rangle$ and $\langle \Phi_\ell | S_\ell^2, \Omega_\ell^2, \Phi_\ell < 0 \rangle$, respectively. (*c,d*) The logarithm base 10 of the number of samples on the S_ℓ^2, Ω_ℓ^2 map (out of a total of 2×10^6 samples). The isolines in (*c,d*) are the values corresponding to the contour.

strongest red region in figure 6(*b*) emerges at the largest S_ℓ^2, while below this threshold, the forward cascade events weaken progressively and are gradually cancelled out by the inverse cascade. Finally, in regions characterized by a weak strain rate and strong rotation rate, the inverse cascade becomes the dominant contribution.

Figures 8(*c,d*) display the distribution of the number of samples corresponding to positive and negative cascade rates in logarithmic scale (out of the 2 million samples (balls) considered). Our focus is directed specifically towards the bottom right corners of the plots, which correspond to the region where the inverse cascade is observed in figure 6(*b*). Interestingly, we observe that at $\Omega_\ell^2/\langle Q_w \rangle \approx 40$ and $S_\ell^2/\langle Q_w \rangle < 10$, the numbers of samples representing both inverse and forward cascade rates are approximately equivalent, falling within the range 10^1–$10^{1.5}$. This implies that within this region, the magnitude of the inverse cascade must be significant to achieve net negative values for the conditional average. Still, for the conditions with net inverse cascade, the number of occurrences for both forward and inverse cascade rates is quite small, of the order of only $1/10^5$ of the total samples, indicating a very low frequency. We point out that in the extreme bins, the conditionally averaged fluxes are unlikely to be fully converged. Therefore, our observations are meant to be mostly qualitative in these regions. In particular, the inverse cascade regions depicted in figure 6 are attributed primarily to rare but intense events. In the next subsection, we will show that inverse cascade can be better characterized by conditioning on Q_ℓ and R_ℓ invariants.

5.2. *Conditional statistics based on Q_ℓ and R_ℓ invariants*

In the context of the Ω_ℓ^2 and S_ℓ^2 map shown in figure 6, we observe the presence of a distinct inverse energy cascade in the region characterized by strong rotation but weak
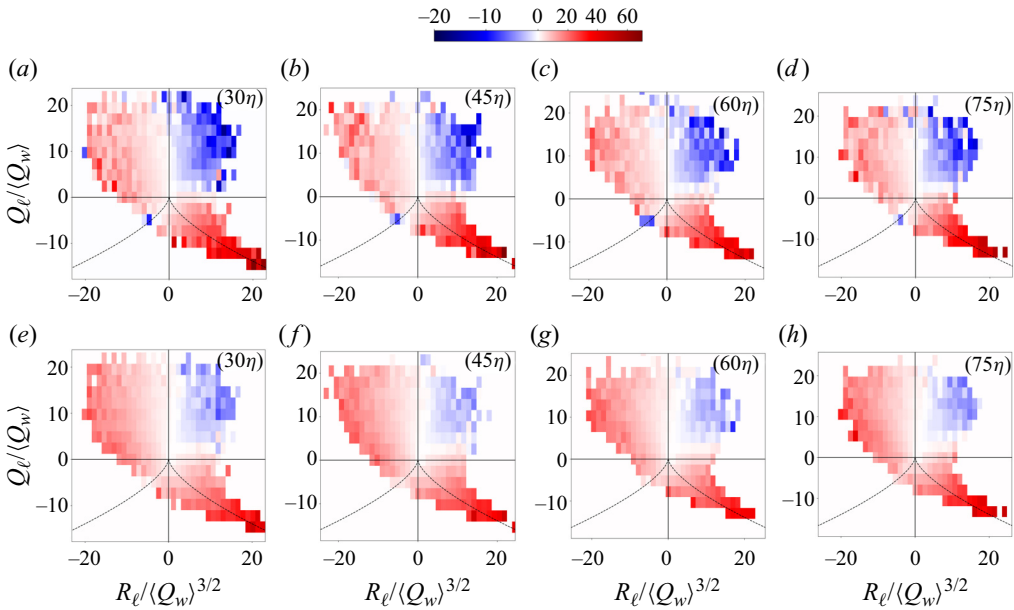
980 A42-16

Figure 9. Plots of (*a–d*) $\langle \Phi_\ell | Q_\ell, R_\ell \rangle$ and (*e–h*) $\langle \Pi_\ell | Q_\ell, R_\ell \rangle$ at $\ell = \{30, 45, 60, 75\}\eta$. The black solid lines separate the four quadrants, and the two lines $Q = -(\frac{27}{4}R^2)^{1/3}$ (Vieillefosse lines) are also shown. Here, Φ_ℓ and Π_ℓ are normalized by $\langle \epsilon \rangle$; Q_ℓ is normalized by $\langle Q_w \rangle$; and R_ℓ is normalized by $\langle Q_w \rangle^{3/2}$. The data and editable analysis code that generated these joint p.d.f.s (for the case at $\ell = 45\eta$) can be found at https://www.cambridge.org/S0022112023010662/JFM-Notebooks/files/figure9.

strain (corresponding to large Q_ℓ values) for Φ_ℓ. However, such observations did not hold for Π_ℓ. But these results do not preclude the possibility that net forward and inverse cascade may be associated with other invariants of the filtered velocity gradient tensor $\tilde{A}_{ij}$.

Figure 9 shows the joint conditionally averaged $\langle \Phi_\ell | Q_\ell, R_\ell \rangle$ and $\langle \Pi_\ell | Q_\ell, R_\ell \rangle$ at four different scales, namely, $\ell = \{30, 45, 60, 75\}\eta$. Across all plots, we can observe the distinctive teardrop-shape pattern on the Q–R map, as reported in previous studies (Chong *et al.* 1990; Meneveau 2011). The black solid lines are the boundaries, separating the four quadrants based on the signs of Q_ℓ and R_ℓ. Notably, it becomes evident that both Φ_ℓ and Π_ℓ exhibit a strong and dominant inverse cascade in the quadrant characterized by $Q_\ell > 0$ and $R_\ell > 0$. It is useful to recall that the variable R_ℓ is associated with the rate of change of Q_ℓ (in fact, assuming restricted Euler dynamics, they are related by $dQ_\ell/dt = -3R_\ell$; Cantwell 1992; Meneveau 2011). Therefore $R_\ell > 0$ corresponds to a decreasing trend of Q_ℓ, i.e. vortex compression. We find that such events are associated with inverse energy cascade. This observation is particularly interesting considering the absence of an observable inverse cascade for Π_ℓ in the S_ℓ^2 and Ω_ℓ^2 map. Hence these results indicate that the variables Q_ℓ and R_ℓ provide a more effective characterization to identify inverse cascade using conditional averaging.

The region characterized by $Q_\ell < 0$ and $R_\ell > 0$, which corresponds to the strain-dominated region, exhibits the most pronounced forward cascade. This observation aligns with the findings of many prior analyses in the literature (Borue & Orszag 1998; van der Bos *et al.* 2002; Carbone & Bragg 2020; Johnson 2021) as well as those depicted in figure 9, further emphasizing that the strong local strain rate plays a crucial role in driving the forward energy cascade. We note that Borue & Orszag (1998) and van der
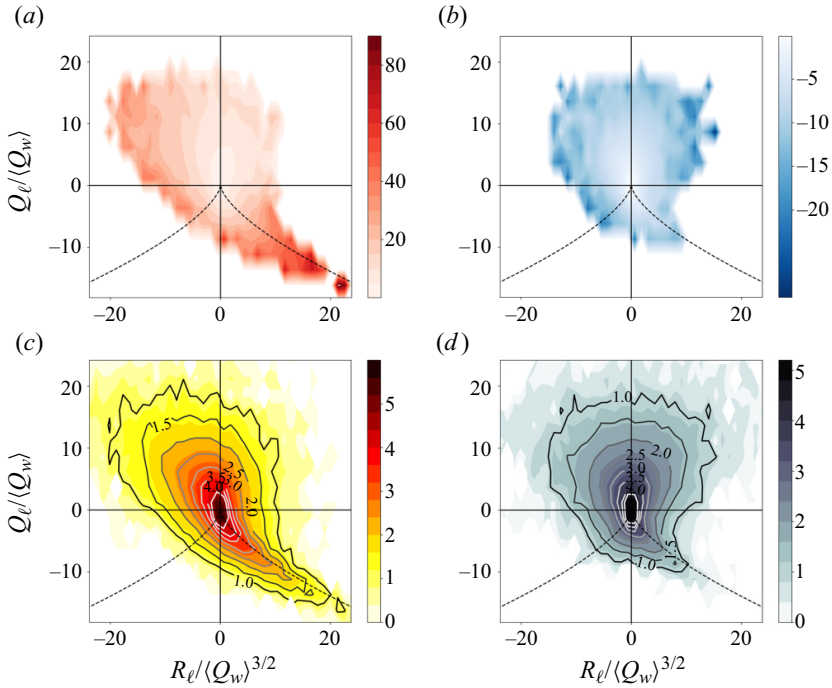
Figure 10. (*a,b*) Plots of $\langle \Phi_\ell | Q_\ell, R_\ell, \Phi_\ell > 0 \rangle$ and $\langle \Phi_\ell | Q_\ell, R_\ell, \Phi_\ell < 0 \rangle$. (*c,d*) Plots of the logarithm base 10 of the number of samples on the Q_ℓ, R_ℓ map. The isolines in (*c,d*) are the values corresponding to the contours.

Bos *et al.* (2002) display conditional averages weighted by the joint p.d.f. of R_ℓ and Q_ℓ. In their results, there was hardly any indication of backscatter/inverse cascade in the $Q_\ell > 0$ and $R_\ell > 0$ 'vortex compression' region, because the overall probability density of that region is smaller than for the other regions. However, the unweighted conditional averaging represents the relevant values if the large-scale flow is in that particular state ($Q_\ell > 0$ and $R_\ell > 0$), and is therefore relevant to our analysis. We also notice a small blue region in the $Q_\ell < 0$, $R_\ell < 0$ quadrant of $\langle \Phi_\ell | Q_\ell, R_\ell \rangle$ (but not seen for $\langle \Pi_\ell | Q_\ell, R_\ell \rangle$). The occurrence of inverse cascade in strain-dominated, strain self-stretching regions appears intriguing. However, the small number of samples ($\sim O(10)$) in the bin showing inverse cascade precludes us from ascribing much significance to this observation for now.

In a manner similar to that in figure 8, we perform further conditional averaging, also distinguishing positive and negative cascade rates. Figures 10(*a,b*) present $\langle \Phi_\ell | Q_\ell, R_\ell, \Phi_\ell > 0 \rangle$ and $\langle \Phi_\ell | Q_\ell, R_\ell, \Phi_\ell < 0 \rangle$ at $\ell = 45\eta$. In the case of the inverse cascade, it is observed to occur in all four quadrants (figure 10*b*), with a more evenly distributed and symmetric presence in the upper two quadrants associated with $Q_\ell > 0$, i.e. the rotation-dominated regions. The characteristic teardrop shape is less prominent and exhibits a shorter tail compared to the forward cascade (figure 10*a*). Regarding the forward cascade, it is evident that it is most dominant in the $Q_\ell < 0$, $R_\ell > 0$ quadrant, consistent with figure 9. However, in the $Q_\ell > 0$, $R_\ell > 0$ quadrant, the forward cascade is weaker and is overall cancelled out by the stronger inverse cascade in that particular region.

Figures 10(*c,d*) display the distributions of number of samples of forward and inverse cascade rates, respectively. The shapes of the distributions align with figures 10(*a,b*), but a
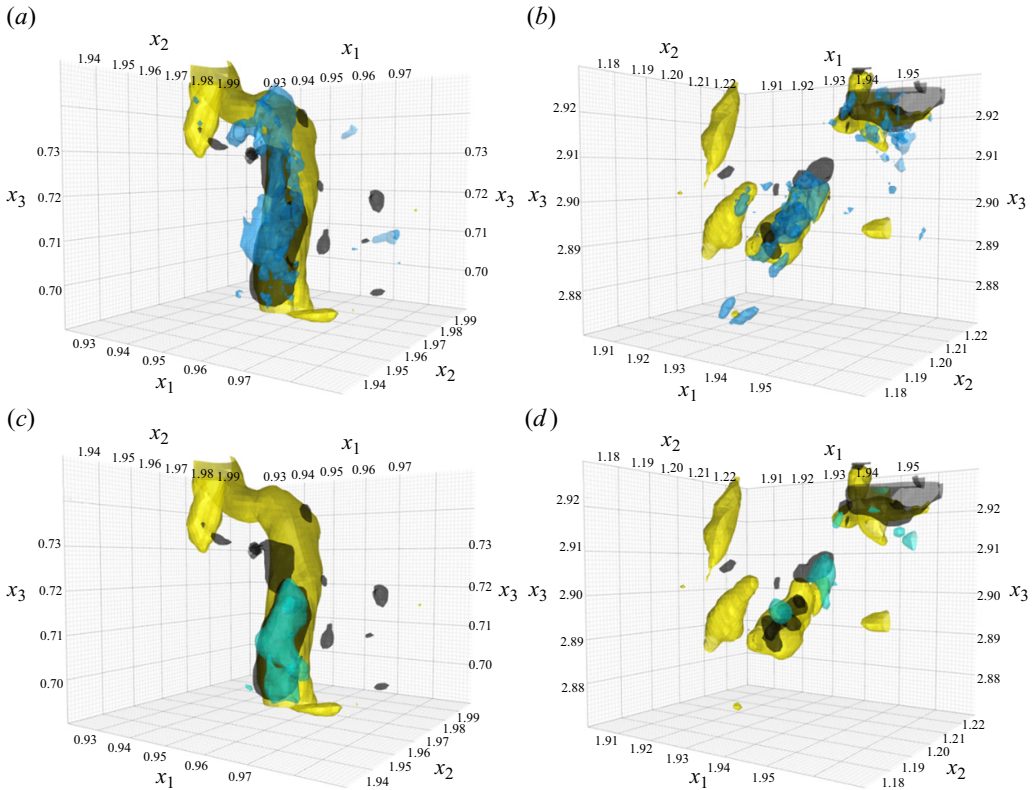
980 A42-18

Figure 11. (*a,b*) Isosurfaces of local $\Phi_\ell/\langle\epsilon\rangle = -60$ (light blue), $Q_\ell/\langle Q_w\rangle = 20$ (yellow) and $R_\ell/\langle Q_w\rangle^{3/2} = 30$ (black) in two different 3-D subdomains. (*c,d*) Isosurfaces of local $\Pi_\ell/\langle\epsilon\rangle = -20$ (green-blue) in the same subdomains and isosurface of $Q_\ell/\langle Q_w\rangle$ and $R_\ell/\langle Q_w\rangle^{3/2}$ as in (*a,b*). Interactive visualizations are available for each panel at Panel (a), Panel (b), Panel (c), Panel (d). The link to the directory containing the visualization code and the 3-D fields for these data can be found at https://www.cambridge.org/S0022112023010662/JFM-Notebooks/files/figure11.

majority of the samples are concentrated at the centre, corresponding to small values of Q_ℓ and R_ℓ. This observation confirms that the strong instances of inverse cascade and forward cascade observed in figure 9 are determined primarily by infrequent but extreme events (intermittency). Note that the joint p.d.f. in figure 10(*d*) is more left–right symmetric than that in figure 10(*c*), suggesting a less non-Gaussian behaviour of the flow in regions of inverse cascade than in the forward cascade regions.

Finally, to provide a visual impression of the spatial distribution of regions of negative Φ_ℓ in the flow, in figure 11 we provide a 3-D visualization of two instances in specific small subdomains of size 150^3 grid points (i.e. $(225\eta)^3$ out of the overall 8192^3 DNS domain. The selection of these subdomains was based on the condition that $Q_\ell/\langle Q_w\rangle > 15$ and $R_\ell/\langle Q_w\rangle^{3/2} > 15$ at the centre of each subdomain, such that the centre is at a strong vortex compression region. We then calculate the values of Φ_ℓ, Π_ℓ, Q_ℓ and R_ℓ at every second grid point. In figures 11(*a,b*), the light blue regions correspond to the isosurface of a large negative value of $\Phi_\ell/\langle\epsilon\rangle = -60$, indicating the presence of an inverse cascade with significant magnitude. Clearly, we can see that the occurrence of a strong inverse cascade is associated closely with the presence of the vortices. Figure 11(*a*) depicts that large negative Φ_ℓ appears near the centre and not at the core of the yellow tube,

980 A42-19

although one should recall that $\Phi_\ell(x, t)$ is defined locally as centred at x but represents the energy cascade into balls of diameter 45η, i.e. comparable to the diameter of the vortex (yellow region) shown. The blue region is also largely connected with the black isosurface ($R_\ell = 20\langle Q_w \rangle^{3/2}$), indicating a strong 'vortex compression' region within the yellow tube. Interactive 3-D versions of the figure that can be accessed following the links in the figure caption help to elucidate the spatial structure. Figure 11(*b*) is an entirely different instance of similar conditions, showing a more broken up vortex, and showing that Φ_ℓ can also peak near the sides, and appear more scattered within the vortex. Coupled with the results shown in figure 9, the visualizations suggest that the strong inverse cascade occurs along the large-scale vortices, in regions of these vortices in which $R_\ell > 0$, i.e. the vortex compression regions. We can also observe some yellow tubes, within which inverse cascade and compression are both absent. This is consistent with the statistics such that when conditionally averaging in terms of Q_ℓ but irrespective of R_ℓ, the inverse cascade becomes very weak and almost non-existent. However, once one considers only $R_\ell > 0$ regions, inverse cascade can be observed clearly in high vortical regions.

We also show $\Pi_\ell/\langle\epsilon\rangle = -20$ (green-blue isosurface) in the corresponding 3-D subdomains shown as figures 11(*c,d*). Clearly, we can see that the green-blue and black regions largely overlap within the yellow region in figure 11(*c*). In figure 11(*d*), the overlapping between green-blue, yellow and black regions occurs at the centre and top right region of the subdomain, indicating that strong negative Π_ℓ is also associated with strong vortex compression within a high vortical region, consistent with figure 9. However, the patterns of the green SGS flux regions are smoother, consistent with the two-dimensional visualisation in figure 5.

Caution must be expressed that visualizations provide only qualitative impressions, and more quantitative analysis requires structure-based conditional averaging, such as undertaken recently in Park & Lozano-Duran (2023). While such analysis is beyond the scope of the present paper, the conditional statistics presented in figure 9 already by themselves provide the strong statistically robust connection between cascade rate measures and features of the large-scale velocity gradient tensor.

6. Conclusions

In this paper, we explore, based on a DNS dataset of isotropic forced turbulence at a relatively high Reynolds number ($R_\lambda = 1250$), local features of the energy cascade. We compare two common definitions of the spatially local rate of kinetic energy cascade at some scale ℓ. The first is based on the cubic velocity difference term appearing in the scale-integrated local KH equation, in the structure-function approach. The second is the subfilter-scale (SFS) energy flux term in the transport equation for subgrid-scale kinetic energy, i.e. as used in the filtering approach often invoked in LES. Particular attention is placed on interpretation and statistical robustness of observations of local negative structure-function energy flux and SFS energy flux. The notion and relevance of local inverse cascade or 'backscatter' has been open to debates in the literature. We argue that the interpretation of $\Phi_\ell(x, t)$ as a spatially local energy flux appears unambiguous because it arises naturally from a divergence term in scale space. And the symmetric formulation of Hill (2001, 2002) leads to the spherically averaged third-order structure function based definition of a local cascade rate involving velocities at two points that are treated equally via angular averaging over the sphere.

The data confirm the presence of local instances where $\Phi_\ell(\boldsymbol{x}, t)$ is negative, i.e. indicative of local inverse cascade events in 3-D turbulence. Flow visualizations show that spatially, the inverse cascade events are often located near the core of large-scale vortex structures. Comparable observations for the LES-based energy flux $\Pi_\ell(\boldsymbol{x}, t)$ (which also displays negative values at many locations in the flow, as is well-known in the LES literature on 'backscatter') show that $\Pi_\ell(\boldsymbol{x}, t)$ displays smoother and more blob-like features. Regarding the statistical significance of such observations, local observations from single realizations are extended using conditional averaging. Attention is placed first on relationships between the local cascade rate and the local filtered viscous dissipation rate $\epsilon_\ell(\boldsymbol{x}, t)$ that plays a central role in the classic KRSH (Kolmogorov 1962). Results show that conditional averaging of both $\Phi_\ell(\boldsymbol{x}, t)$ and $\Pi_\ell(\boldsymbol{x}, t)$ eliminates negative values, and that the conditional averages in fact equate $\epsilon_\ell(\boldsymbol{x}, t)$ to very good approximation, entirely consistent with KRSH predictions.

The analysis then focuses on conditional averages of Φ_ℓ and Π_ℓ conditioned on properties of the filtered velocity gradient tensor properties, in particular four of its most important invariants (strain and rotation rate square magnitude, and the two Q–R invariants). We find statistically robust evidence of inverse cascade as measured with Φ_ℓ when both the large-scale rotation rate is strong and the large-scale strain rate is weak. When defined using Π_ℓ, the conditional averaging based on large-scale strain and rotation rates does not lead to any significant average backscatter. When conditioning based on the R_ℓ and Q_ℓ invariants, significant net inverse cascading is observed for Φ_ℓ in the 'vortex compression' $R_\ell > 0$, $Q_\ell > 0$ quadrant. Qualitatively similar, but quantitatively much weaker trends are observed for the conditionally averaged SFS energy flux Π_ℓ. We recall that a multiscale decomposition of Π_ℓ in terms of velocity gradients at multiple scales (Johnson 2020, 2021) shows that $\Pi_\ell < 0$ appears associated with a vortex-thinning mechanism occurring at smaller scales interacting with large-scale strains.

In summary, present results show that locally negative values of kinetic energy fluxes at scale ℓ are observed for both the structure-function and filtering approaches, and at least for the structure-function approach, the interpretation as a flux in scale space appears unambiguous. Regarding statistical robustness and the potential net impact of such local observations, conditional averaging reveals that both negative Φ_ℓ and negative Π_ℓ (representing inverse cascade) become statistically dominant mechanisms in regions where turbulent motions at scales larger than ℓ exhibit a 'vortex compression' behaviour ($R_\ell > 0$ and $Q_\ell > 0$). However, the magnitude of inverse cascade in filtering approaches is weaker and negligible on the $(S_\ell^2, \Omega_\ell^2)$ map.

For future work, it would be of interest to explore the sensitivity of results to Reynolds number, especially as it is expected that at higher Reynolds numbers, the intermittency of the variables would increase. It would be also interesting to extend conditional averaging to more accurately reflect local energy distribution, entire flow structures and their possible connections to local inverse cascade mechanisms. Other pointwise quantities such as helicity can also be explored. It would also be instructive to connect present results with the multiscale decomposition of Johnson (2020, 2021), and thus be able to identify the small-scale mechanisms associated with local backscatter/inverse cascade events. And further theoretically obtained exact relations between structure-function and filtering approaches may yet be found.

Author ORCIDs.

- Hanxun Yao https://orcid.org/0009-0004-7255-4843;
- Michael Schnaubelt https://orcid.org/0000-0001-8617-894X;
- Tamer A. Zaki https://orcid.org/0000-0002-1979-7748;
- Charles Meneveau https://orcid.org/0000-0001-6947-3605.

Appendix A. Turbulence database access tools

The high-resolution isotropic DNS data are accessible via new Python-based tools built upon the data housed in the JHTDB (Li *et al.* 2008). The JHTDB has been operating for over a decade and has led to hundreds of peer-reviewed articles on turbulence. A new set of data access tools based on Jupyter Notebooks has been developed that enables direct access to subsets of the data continuing the 'virtual sensors' concept (Li *et al.* 2008). The new notebooks provide fast and stable operation on the existing turbulence datasets while enabling user-programmable, server-side computations. To date, the new data access tools have been implemented and tested on the high Reynolds number, forced isotropic turbulence dataset on 8192^3 grid points (the isotropic8192 datasets) of which five snapshots are at a Taylor microscope Reynolds number $Re_\lambda = 1250$ (Yeung *et al.* 2012), and one with very high spatial resolution at $Re_\lambda = 610$.

The isotropic8192 dataset has been partitioned into 4096 Zarr database files, each of which is a 512^3 volume cubelet of the 8192^3 data. Each Zarr file stores the velocity and pressure variables in distinct Zarr groups, and the data in each group are broken down further into chunks. The chunks are ijk-ordered such that cutouts and interpolation buckets, the size of which are dependent on the interpolation or differentiation method selected by the user, can be cut out directly from the intersecting chunk(s).

The new Python-based data access tools, pyturb, are accessed via the SciServer (sciserver.org) platform. Pyturb interfaces directly with the data files in Zarr format, stored on volumes mounted to each user's SciServer container. The entirety of the isotropic8192 dataset (8192^3 volume, six snapshots) in Zarr format is available publicly through Python Notebook on SciServer. Users can apply for a SciServer account freely, and download the demo Notebook. In the Notebook, users can get access to pre-coded 'Get' functions for arbitrary sets of points: GetPressure to retrieve and interpolate pressures, GetPressureGradient to retrieve and interpolate pressure gradient, and similarly GetPressureHessian, GetVelocity, GetVelocityGradient, GetVelocityHessian, GetVelocityLaplacian and GetCutout to read raw data for a user-specified box.

Demo codes for accessing data at user-specified arrays of points (in various sample geometrical configurations) are listed in the Notebook. The isotropic8192 datasets can be also accessed via the web-portal cutout service where the pyturb GetCutout function has replaced the legacy function for user queries (see https://turbulence.pha. jhu.edu/newcutout.aspx). The JHTDB still provides and maintains other datasets (https:// turbulence.pha.jhu.edu/datasets.aspx) through legacy SQL systems with C, Fortran, Matlab, Python and .Net interfaces. However, the aim is to transfer the existing datasets and any newcoming datasets to the pyturb system in the future for faster and more stable services.

Appendix B. Evaluating and comparing $\langle k_{sf,\ell} \rangle$ and $\langle k_{sgs,\ell} \rangle$

The average values $\langle k_{sf,\ell} \rangle$ and $\langle k_{sgs,\ell} \rangle$ can be obtained from classical turbulence theory and the Kolmogorov spectrum. To evaluate $\langle k_{sf,\ell} \rangle$, we use the general expression for the structure-function tensor in isotropic turbulence in the inertial range

$$\langle \delta u_i(\boldsymbol{r})\, \delta u_j(\boldsymbol{r}) \rangle = C_2 \langle \epsilon \rangle^{2/3} r^{2/3} \left(\frac{4}{3} \delta_{ij} - \frac{1}{3} \frac{r_i r_j}{r^2} \right), \tag{B1}$$

and write

$$\langle k_{sf,\ell} \rangle = \frac{1}{2V_\ell} \iiint_{V_\ell} \frac{1}{2} \langle \delta u_i^2(\boldsymbol{r}) \rangle \, \mathrm{d}^3 \boldsymbol{r}_s = \frac{1}{4} \frac{1}{V_\ell} \iiint_{V_\ell} C_2 \langle \epsilon \rangle^{2/3} r^{2/3} \left(\frac{4}{3} \delta_{ii} - \frac{1}{3} \frac{r_i r_i}{r^2} \right) \mathrm{d}^3 \boldsymbol{r}_s, \tag{B2}$$

where $\boldsymbol{r}_s = \boldsymbol{r}/2$. The integration yields

$$\langle k_{sf,\ell} \rangle = \frac{C_2 \langle \epsilon \rangle^{2/3} \ell^{2/3}}{4 \times 3\pi(\ell/2)^3/4} \int_0^{\ell/2} 4\pi r_s^2 (2r_s)^{2/3} \, \mathrm{d}r_s = \frac{3}{4} C_2 \langle \epsilon \rangle^{2/3} \ell^{2/3} \approx 1.6 \langle \epsilon \rangle^{2/3} \ell^{2/3} \quad \text{(B3)}$$

when using the usual empirical Kolmogorov structure-function constant $C_2 \approx 2.1$.

In order to evaluate $\langle k_{sgs,\ell} \rangle$, we use (Pope 2000; Li & Meneveau 2004)

$$\langle \tau_{ij} \rangle = \iiint \left(1 - \hat{G}_\ell^2(\boldsymbol{k}) \right) \Phi_{ij}(\boldsymbol{k}) \, \mathrm{d}^3 \boldsymbol{k} \overset{(i=j)}{=} C_K \langle \epsilon \rangle^{2/3} \int_0^\infty \left(1 - \hat{G}_\ell^2(\boldsymbol{k}) \right) 2k^{-5/3} \, \mathrm{d}k, \quad \text{(B4)}$$

where $\hat{G}_\ell(\boldsymbol{k}) = \hat{G}_\ell(k)$ is the Fourier transform of the filter function at scale ℓ, and $\Phi_{ij}(\boldsymbol{k}) = E(k)/(4\pi k^2)(\delta_{ij} - k_i k_j/k^2)$ is the spectral tensor for isotropic turbulence, while $E(k) = C_K \langle \epsilon \rangle^{2/3} k^{-5/3}$ is the radial 3-D energy spectrum of turbulence.

For the spherical top-hat filter, its Fourier transform can be shown to be

$$\hat{G}_\ell(k) = \frac{3}{(k\ell/2)^3} \left(\sin \frac{k\ell}{2} - \frac{k\ell}{2} \cos \frac{k\ell}{2} \right), \tag{B5}$$

where $k = |\boldsymbol{k}|$. The definite integral needed to evaluate the right-hand side of (B4) exists (using WolframAlpha online) and is given by

$$\int_0^\infty \left(1 - \left[\frac{3}{(\kappa/2)^3} \left(\sin \frac{\kappa}{2} - \frac{\kappa}{2} \cos \frac{\kappa}{2} \right) \right]^2 \right) \kappa^{-5/3} \, \mathrm{d}\kappa = -544\, \Gamma(-20/3), \tag{B6}$$

with $\kappa = k\ell$ and where $\Gamma(\cdot)$ is the gamma function. Evaluating and using $C_K \approx 1.6$, the result is

$$\langle k_{sgs,\ell} \rangle = \tfrac{1}{2} \langle \tau_{ii} \rangle = 0.76\, C_K \langle \epsilon \rangle^{2/3} \ell^{2/3} \approx 1.2\, \langle \epsilon \rangle^{2/3} \ell^{2/3}. \tag{B7}$$

As can be seen, the 3-D integration needed to evaluate $\langle k_{sf} \rangle$ involves the radius to the 8/3 power, while that for $\langle k_{sgs} \rangle$ involves the wavenumber to the $-5/3$ power. The former is thus much more strongly dominated by the large-scale limit of integration ($\ell/2$) than the latter. As a result, the latter is more strongly affected by the spectral behaviour of turbulence at smaller scales, including the viscous range. This explains why the values of $\langle k_{sgs} \rangle$ measured from DNS are significantly smaller than the prediction in (B7), while the measurements of $\langle k_{sf} \rangle$ agree well with the prediction in (B3).

REFERENCES

ANTONIA, R.A., ZHOU, T., DANAILA, L. & ANSELMET, F. 2000 Streamwise inhomogeneity of decaying grid turbulence. *Phys. Fluids* **12** (11), 3086–3089.

BALLOUZ, J.G. & OUELLETTE, N.T. 2018 Tensor geometry in the turbulent cascade. *J. Fluid Mech.* **835**, 1048–1064.

BARDINA, J., FERZIGER, J.H. & ROGALLO, R.S. 1985 Effect of rotation on isotropic turbulence: computation and modelling. *J. Fluid Mech.* **154**, 321–336.

BORUE, V. & ORSZAG, S.A. 1998 Local energy flux and subgrid-scale statistics in three-dimensional turbulence. *J. Fluid Mech.* **366**, 1–31.

VAN DER BOS, F., TAO, B., MENEVEAU, C. & KATZ, J. 2002 Effects of small-scale turbulent motions on the filtered velocity gradient tensor as deduced from holographic particle image velocimetry measurements. *Phys. Fluids* **14** (7), 2456–2474.

BUARIA, D. & PUMIR, A. 2022 Vorticity-strain rate dynamics and the smallest scales of turbulence. *Phys. Rev. Lett.* **128** (9), 094501.

CANTWELL, B.J. 1992 Exact solution of a restricted Euler equation for the velocity gradient tensor. *Phys. Fluids* A*: Fluid Dyn.* **4** (4), 782–793.

CARBONE, M. & BRAGG, A.D. 2020 Is vortex stretching the main cause of the turbulent energy cascade? *J. Fluid Mech.* **883**, R2.

CERUTTI, S. & MENEVEAU, C. 1998 Intermittency and relative scaling of subgrid-scale energy dissipation in isotropic turbulence. *Phys. Fluids* **10** (4), 928–937.

CHONG, M.S., PERRY, A.E. & CANTWELL, B.J. 1990 A general classification of three-dimensional flow fields. *Phys. Fluids* A*: Fluid Dyn.* **2** (5), 765–777.

CIMARELLI, A., DE ANGELIS, E. & CASCIOLA, C.M. 2013 Paths of energy in turbulent channel flows. *J. Fluid Mech.* **715**, 436–451.

CIMARELLI, A., MOLLICONE, J.-P., VAN REEUWIJK, M. & DE ANGELIS, E. 2021 Spatially evolving cascades in temporal planar jets. *J. Fluid Mech.* **910**, A19.

CONSTANTIN, P., WEINAN, E. & TITI, E.S. 1994 Onsager's conjecture on the energy conservation for solutions of Euler's equation. *Commun. Math. Phys.* **165**, 207–209.

DANAILA, L., ANSELMET, F. & ZHOU, T. 2004 Turbulent energy scale-budget equations for nearly homogeneous sheared turbulence. *Flow Turbul. Combust.* **72**, 287–310.

DANAILA, L., ANSELMET, F., ZHOU, T. & ANTONIA, R.A. 2001 Turbulent energy scale budget equations in a fully developed channel flow. *J. Fluid Mech.* **430**, 87–109.

DANAILA, L., KRAWCZYNSKI, J.F., THIESSET, F. & RENOU, B. 2012 Yaglom-like equation in axisymmetric anisotropic turbulence. *Physica* D **241** (3), 216–223.

DANISH, M. & MENEVEAU, C. 2018 Multiscale analysis of the invariants of the velocity gradient tensor in isotropic turbulence. *Phys. Rev. Fluids* **3** (4), 044604.

DAVIDSON, P.A. 2015 *Turbulence: An Introduction for Scientists and Engineers*. Oxford University Press.

DUBRULLE, B. 2019 Beyond Kolmogorov cascades. *J. Fluid Mech.* **867**, P1.

DUCHON, J. & ROBERT, R. 2000 Inertial energy dissipation for weak solutions of incompressible Euler and Navier–Stokes equations. *Nonlinearity* **13** (1), 249–255.

EYINK, G.L. 1995 Local energy flux and the refined similarity hypothesis. *J. Stat. Phys.* **78**, 335–351.

EYINK, G.L. 2002 Local 4/5-law and energy dissipation anomaly in turbulence. *Nonlinearity* **16** (1), 137.

EYINK, G.L. 2006 Multi-scale gradient expansion of the turbulent stress tensor. *J. Fluid Mech.* **549**, 159–190.

EYINK, G.L. & ALUIE, H. 2009 Localness of energy cascade in hydrodynamic turbulence. I. Smooth coarse graining. *Phys. Fluids* **21** (11), 115107.

EYINK, G.L. & SREENIVASAN, K.R. 2006 Onsager and the theory of hydrodynamic turbulence. *Rev. Mod. Phys.* **78** (1), 87 (see also link to Onsager's unpublished notes at https://ntnu.tind.io/record/121183, in particular slides 14–19).

FRISCH, U. 1995 *Turbulence: The Legacy of AN Kolmogorov*. Cambridge University Press.

GERMANO, M. 1992 Turbulence: the filtering approach. *J. Fluid Mech.* **238**, 325–336.

GOMES-FERNANDES, R., GANAPATHISUBRAMANI, B. & VASSILICOS, J.C. 2015 The energy cascade in near-field non-homogeneous non-isotropic turbulence. *J. Fluid Mech.* **771**, 676–705.

GOTO, S. 2008 A physical mechanism of the energy cascade in homogeneous isotropic turbulence. *J. Fluid Mech.* **605**, 355–366.

HILL, R.J. 2001 Equations relating structure functions of all orders. *J. Fluid Mech.* **434**, 379–388.

HILL, R.J. 2002 Exact second-order structure-function relationships. *J. Fluid Mech.* **468**, 317–326.

JOHNSON, P.L. 2020 Energy transfer from large to small scales in turbulence by multiscale nonlinear strain and vorticity interactions. *Phys. Rev. Lett.* **124** (10), 104501.

JOHNSON, P.L. 2021 On the role of vorticity stretching and strain self-amplification in the turbulence energy cascade. *J. Fluid Mech.* **922**, A3.

KERR, R.M., DOMARADZKI, J.A. & BARBIER, G. 1996 Small-scale properties of nonlinear interactions and subgrid-scale energy transfer in isotropic turbulence. *Phys. Fluids* **8** (1), 197–208.

KOLMOGOROV, A.N. 1941 The local structure of turbulence in incompressible viscous fluid for very large Reynolds numbers. *CR Acad. Sci. URSS* **30**, 301–305.

KOLMOGOROV, A.N. 1962 A refinement of previous hypotheses concerning the local structure of turbulence in a viscous incompressible fluid at high Reynolds number. *J. Fluid Mech.* **13** (1), 82–85.

LANGFORD, J.A. & MOSER, R.D. 1999 Optimal LES formulations for isotropic turbulence. *J. Fluid Mech.* **398**, 321–346.

LEONARD, A. 1975 Energy cascade in large-eddy simulations of turbulent fluid flows. In *Advances in Geophysics*, vol. 18, pp. 237–248. Elsevier.

LI, Y. & MENEVEAU, C. 2004 Analysis of mean momentum flux in subgrid models of turbulence. *Phys. Fluids* **16** (9), 3483–3486.

LI, Y., PERLMAN, E., WAN, M., YANG, Y., MENEVEAU, C., BURNS, R., CHEN, S., SZALAY, A. & EYINK, G.L. 2008 A public turbulence database cluster and applications to study Lagrangian evolution of velocity increments in turbulence. *J. Turbul.* **9**, N31.

LILLY, D.K. 1967 The representation of small-scale turbulence in numerical simulation experiments. *IBM Form*, 195–210.

LÜTHI, B., HOLZNER, M. & TSINOBER, A. 2009 Expanding the Q–R space to three dimensions. *J. Fluid Mech.* **641**, 497–507.

MARATI, N., CASCIOLA, C.M. & PIVA, R. 2004 Energy cascade and spatial fluxes in wall turbulence. *J. Fluid Mech.* **521**, 191–215.

MENEVEAU, C. 2010 Turbulence: subgrid-scale modeling. *Scholarpedia* **5** (1), 9489.

MENEVEAU, C. 2011 Lagrangian dynamics and models of the velocity gradient tensor in turbulent flows. *Annu. Rev. Fluid Mech.* **43**, 219–245.

MENEVEAU, C. & KATZ, J. 2000 Scale-invariance and turbulence models for large-eddy simulation. *Annu. Rev. Fluid Mech.* **32** (1), 1–32.

MENEVEAU, C. & SREENIVASAN, K.R. 1991 The multifractal nature of turbulent energy dissipation. *J. Fluid Mech.* **224**, 429–484.

MOLLICONE, J.-P., BATTISTA, F., GUALTIERI, P. & CASCIOLA, C.M. 2018 Turbulence dynamics in separated flows: the generalised Kolmogorov equation for inhomogeneous anisotropic conditions. *J. Fluid Mech.* **841**, 1012–1039.

MOSER, R.D., HAERING, S.W. & YALLA, G.R. 2021 Statistical properties of subgrid-scale turbulence models. *Annu. Rev. Fluid Mech.* **53**, 255–286.

PARK, D. & LOZANO-DURAN, A. 2023 The coherent structure of the energy cascade in isotropic turbulence. *J. Fluid Mech.* (submitted) arXiv:2306.08784.

PIOMELLI, U., CABOT, W.H., MOIN, P. & LEE, S. 1991 Subgrid-scale backscatter in turbulent and transitional flows. *Phys. Fluids* A*: Fluid Dyn.* **3** (7), 1766–1771.

POPE, S.B. 2000 *Turbulent Flows*. Cambridge University Press.

PORTELA, F.A., PAPADAKIS, G. & VASSILICOS, J.C. 2017 The turbulence cascade in the near wake of a square prism. *J. Fluid Mech.* **825**, 315–352.

RICHARDSON, L.F. 1922 *Weather Prediction by Numerical Process*. Cambridge University Press.

STOLOVITZKY, G., KAILASNATH, P. & SREENIVASAN, K.R. 1992 Kolmogorov's refined similarity hypotheses. *Phys. Rev. Lett.* **69** (8), 1178.

TAO, B., KATZ, J. & MENEVEAU, C. 2002 Statistical geometry of subgrid-scale stresses determined from holographic particle image velocimetry measurements. *J. Fluid Mech.* **457**, 35–78.

VELA-MARTÍN, A. 2022 Subgrid-scale models of isotropic turbulence need not produce energy backscatter. *J. Fluid Mech.* **937**, A14.

VELA-MARTÍN, A. & JIMÉNEZ, J. 2021 Entropy, irreversibility and cascades in the inertial range of isotropic turbulence. *J. Fluid Mech.* **915**, A36.

VIEILLEFOSSE, P. 1982 Local interaction between vorticity and shear in a perfect incompressible fluid. *J. Phys.* **43** (6), 837–842.

VREMAN, B., GEURTS, B. & KUERTEN, H. 1994 Realizability conditions for the turbulent stress tensor in large-eddy simulation. *J. Fluid Mech.* **278**, 351–362.

YAO, H., MOLLICONE, J.-P. & PAPADAKIS, G. 2022 Analysis of interscale energy transfer in a boundary layer undergoing bypass transition. *J. Fluid Mech.* **941**, A14.

YAO, H. & PAPADAKIS, G. 2023 On the role of the laminar/turbulent interface in energy transfer between scales in bypass transition. *J. Fluid Mech.* **960**, A24.

YAO, H., YEUNG, P.K., ZAKI, T.A. & MENEVEAU, C. 2023 Forward and inverse energy cascade and fluctuation relation in fluid turbulence adhere to Kolmogorov's refined similarity hypothesis. *Phys. Rev. Lett.* (submitted) arXiv:2307.06546.

YASUDA, T. & VASSILICOS, J.C. 2018 Spatio-temporal intermittency of the turbulent energy cascade. *J. Fluid Mech.* **853**, 235–252.

YEUNG, P.K., DONZIS, D.A. & SREENIVASAN, K.R. 2012 Dissipation, enstrophy and pressure statistics in turbulence simulations at high Reynolds numbers. *J. Fluid Mech.* **700**, 5–15.

ZHOU, Y. & VASSILICOS, J.C. 2020 Energy cascade at the turbulent/nonturbulent interface. *Phys. Rev. Fluids* **5** (6), 064604.